ELSEVIER

Contents lists available at ScienceDirect

# Sensors and Actuators: B. Chemical

journal homepage: www.elsevier.com/locate/snb





# Robust acoustofluidic micromixer based on an ultrathin PDMS microballoon oscillator

Yeji Yang , Changsub Shin, Sofonias Nursefa Kedir , Bhargav Krishna Pullagura, Heeyeon Kim, Abdi Mirgissa Kaba, Dohyun Park, Taeksang Lee , Dohyun Kim

Division of Mechanical Systems Engineering, Myongji University, 116 Myongji-ro, Yongin 17058, Republic of Korea

#### ARTICLE INFO

Keywords:
Acoustofluidics
Ultrathin PDMS membrane
3D printing
Microfluidic mixer
Streaming analysis
Finite element method

#### ABSTRACT

We present an acoustofluidic micromixer based on a PDMS microballoon oscillator. Effective mixing is essential for diverse microfluidic applications. Among acoustofluidic techniques, cavitation microstreaming has shown exceptionally rapid mixing. However, its real-world application is limited due to the short operational lifetime of oscillating bubbles. To address this limitation, we introduce a novel device architecture comprising a resonating microballoon formed by an inflated, highly flexible, ultrathin PDMS membrane. The device was fabricated via coating PDMS membranes onto a Petri dish, followed by membrane transfer onto a 3D-printed oscillator body. Using solvent-free spin-coating, we achieved membranes as thin as 860 nm. The mechanical properties of our device were systematically characterized including inflation and deflation behaviors. To balance lifetime and streaming performance, we optimized the operational conditions using high-speed streaming visualization. Effective streaming was sustained over 6 h under the optimal configuration: 40-µm membrane thickness, 0.8-mm microballoon size, and  $60\text{-V}_{pp}$  excitation voltage. The device demonstrated excellent mixing performance, homogenizing a 6-µl ink in 600-µl DI water within 32 s. We also developed a finite element method based on the Yeoh hyperelastic model to guide device design and establish operational limits. Finally, we validated the device's utility by performing DNA extraction. The extracted DNA exhibited concentration, purity, and downstream applicability comparable to a commercial kit, yet with more than threefold throughput. We anticipate that our PDMS microballoon-based micromixer will offer a promising solution for a broad range of microfluidic applications where reliable and efficient mixing is crucial.

# 1. Introduction

Mixing is the mass-transfer process of combining two or more substances to bind or form products [1]. Mixing is a ubiquitous and fundamental function in microfluidic devices for a wide range of applications including bio/-chemical analysis (e.g., nucleic-acid analysis [2], immunoassay [3], environmental analysis [4], sample preparation [5]), synthesis (e.g., isotope labeling [6], nanoparticle production [7], crystallization [8]), and enzymatic reactions (e.g., protein digestion [9], nucleic-acid restriction [10]). However, conventional convective mixing, relying on bulk-fluid movement, is ineffective at the microscale due to the predominance of viscous forces over inertial forces, reflected by low Reynolds numbers (Re<<1) [11,12]. Therefore, developing effective microscale mixing techniques (i.e., microfluidic mixer or micromixer) remains a critical challenge. Despite being a long-standing field, micromixing continues to be an active area of research, as evidenced by

the still-growing body of literature on this topic [13–17].

Microfluidic mixers are largely classified into passive and active types [1,17,18]. Passive mixers exploit diffusion between laminar streams or chaotic advection generated by specific channel geometries [1,17,19]. While they require no external energy input beyond the pressure needed to drive flow, their operation depends on complex microstructures such as staggered herringbone grooves [20], Tesla structures [21], and twisted channels [22], which can be difficult to fabricate. Moreover, passive mixing typically requires high flow rates (Re>1) and pressure, which may increase the risk of leakage [1,23]. A further limitation of passive mixing is the lack of precise control over the extent of mixing [18,24].

In contrast, active mixing employs external energy or stimuli (e.g., thermal [18], acoustic [25], electrokinetic [26], electrohydrodynamic [14]). The active mixers have a relatively simpler geometry (e.g., standard channel or chamber), eliminating the need for intricate internal

E-mail address: dohyun.kim@mju.ac.kr (D. Kim).

<sup>\*</sup> Corresponding author.

structures. More importantly, active mixers offer precise control over mixing behavior [27]. That is, mixing can be rapidly turned on or off, and its intensity can be modulated by adjusting the input stimulus [28]. Such control is particularly advantageous for multistep assays such as DNA extraction, where sequential reagent addition and stage-specific mixing conditions are required [29].

Among the various active mixing strategies, acoustic or acoustofluidic mixing has recently brought significant attention. Acoustofluidic mixing, encompassing Rayleigh streaming [30,31], cavitation microstreaming [29,32], Eckart streaming [33,34], sharp-edge microstreaming [35,36], acoustic plate-mode streaming [37-40], and surface-acoustic wave (SAW) streaming [41,42], utilizes streaming generated at liquid-solid or liquid-gas interfaces under acoustic resonance [43–45]. The acoustofluidic micromixer offers several advantages over other active approaches: (1) exceptionally rapid mixing, with timescales as short as a few tens of milliseconds [27], (2) simplified microfabrication, as streaming can be generated using a piezo actuator (i.e., PZT for bulk acoustic wave) or a piezoelectric substrate (i.e., lithium niobate for SAW) bonded to a microchannel, (3) straightforward operation, controlled by an alternating current (AC) signal generator, and (4) broad compatibility, as performance is largely insensitive to liquid properties (e.g., dielectric or magnetic) and channel-surface characteristics (e.g., electrokinetic).

Among acoustofluidic techniques, cavitation microstreaming has garnered particular interest. It exploits counter-rotating circulatory flows arising from resonating air bubbles [43,46-49]. Cavitation microstreaming has been implemented in various microfluidic applications, including DNA fragmentation [50], immunoassay [51], and DNA extraction [29], owing to its simple implementation, involving bubble-capturing air pockets integrated into a microfluidic chip [29,32, 52]. Furthermore, it champions exceptionally rapid mixing [53,54] as its streaming velocity reaches 100-400 µm/s [55]. However, despite its promise, real-world deployment remains constrained due to a critical drawback: the limited temporal stability of oscillating bubbles. Bubbles often collapse prematurely or air pockets flood unexpectedly due to the inherent instability of the air-liquid interface under acoustic excitation (Fig. 1a) [56,57]. In our previous work, we successfully demonstrated cavitation-microstreaming-based cell lysis and DNA extraction [29]. However, the spontaneous collapse of bubbles (usually <10 min) posed a major barrier to practical application and broader dissemination. To overcome this limitation, we propose a new device architecture as a robust alternative to a fragile air bubble. We hypothesized that a resonating microballoon, an inflated ultrathin PDMS membrane, suspended over a cavity, can generate acoustic streaming while offering a substantially longer lifetime (Fig. 1b).

Previous studies presented acoustic streaming generated by vibrating membranes (or diaphragm) coupled with a cavity, using materials

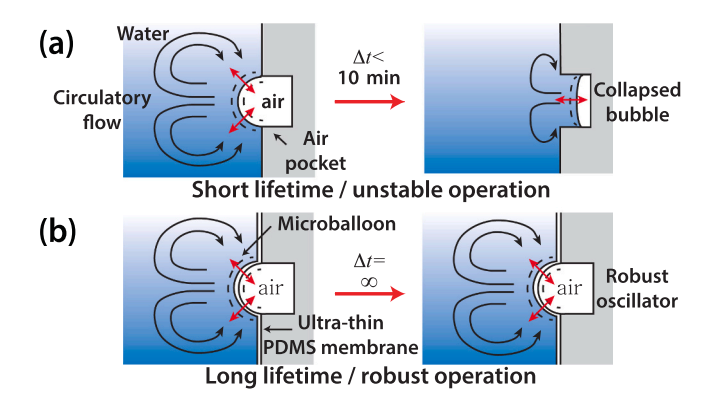


**Fig. 1.** Comparison of stability between (a) cavitation microstreaming generated by an oscillating bubble captured in an air pocket, and (b) acoustic microstreaming produced by a vibrating PDMS microballoon integrated with an air cavity.

including a thin plastic film (the material not specified) [58], low-pressure chemical vapor deposition (LPCVD) silicon nitride with and without perforations [59,60], wet-etched single-crystal silicon [61], and brass membranes [62]. These materials are stiff, indicated by high Young's moduli:thermoplastics (55-420 GPa [63], LPCVD silicon nitride (270 GPa [64]), single crystal silicon (130-188 GPa [65]), and brass (102 GPa [66]). In contrast, PDMS exhibited a significantly lower Young's modulus, ranging from 12 kPa to 2.50 MPa [67–69], a difference of five to seven orders of magnitude. This compliance suggests that PDMS membrane may undergo larger dynamic deformation and stronger vibrations under the same acoustic input, potentially enhancing streaming performance. To the best of our knowledge, this is the first time to employ an ultrathin PDMS microballoon for acoustic streaming. While one previous report described the use of a PDMS membrane bonded to a PZT (lead zirconate titanate) actuator to induce acoustic streaming, it did not incorporate an air cavity to amplify membrane vibration [47,49,70]. Our approach, therefore, represents a novel configuration that leverages the mechanical compliance of PDMS in conjunction with a vibrating, expanded membrane to enhance acoustofluidic performance. A previous work demonstrated a microbubble embedded in a cuboid PDMS chamber for acoustic cell manipulation. However, the microstructure was non-inflatable, limiting their streaming performance [71].

Here, we first fabricated ultrathin PDMS membranes via spin-coating on a polystyrene Petri dish. A PDMS microballoon was formed on a 3D-printed oscillator body using a membrane transfer technique. Key properties of the microballoon were characterized including its pressure-dependent inflation and time-dependent deflation. Next, its acoustofluidic performance was evaluated under various operating conditions using a high-speed streaming visualization, and the optimal parameters for effective and stable streaming were identified. The operational lifetime of the microballoon was assessed based on its ability to sustain streaming over extended periods. A finite-element analysis (FEA) method was developed to guide device design and establish operational limits. A dye homogenization test using an ink droplet was performed to quantify mixing performance. Finally, the DNA extraction was conducted to demonstrate the practical utility of our microfluidic device.

# 2. Materials and methods

#### 2.1. Materials and reagents

Polydimethylsiloxane (PDMS, Sylgard 184) was purchased from Dow Corning (Midland, MI, United States). PlasClear, a transparent resin for digital-light-processing (DLP) 3D printing, was obtained from Asiga (New South Wales, Australia). Polystyrene (PS) Petri dishes, used as a flat mold for PDMS-membrane fabrication, were supplied by SPL Life Science (#10101, Pocheon, South Korea). Black ink used for mixing experiments was sourced from Javapen (Seoul, South Korea).

The MagaZorb DNA Mini-Prep Kit, a commercial DNA-extraction kit based on silica-coated magnetic beads, was obtained from Promega (#0000397378, Madison, WI, United States). Reagents for cell lysis and DNA extraction, including Proteinase K, lysis buffer, washing buffer I, washing buffer II, and elution buffer, were from a QIAamp DNA Mini Kit (Qiagen, Hilden, Germany). MagAttract Suspension G magnetic beads (#1026901) were also purchased from Qiagen. The K562 human chronic myeloid leukemia cell line was acquired from the Korean Cell Line Bank (Seoul, South Korea). RPMI-1640 culture medium and phosphate-buffered saline (PBS, pH 7.4) were obtained from Sigma Aldrich (St. Louis, MO, United States). Ethanol (99.5 %) was obtained from Daejung Chemicals and Metals (Shiheung, South Korea).

Forward and backward primers for PCR (polymerase chain reaction) were synthesized by Macrogen (Seoul, South Korea). PCR amplification was performed using  $2 \times DNA$  free-HotTaq PCR Master Mix (CellSafe, Yongin, South Korea) with nuclease-free DI water (#BW007a,

Biosolution, Suwon, South Korea). Agarose powder (Bio-Rad, Hercules, CA, United States),  $50 \times \text{TAE}$  buffer (#EBT002, Enzynomics, Daejeon, South Korea), Dyne LoadingSTAR fluorescent stain (#A751, DYNE Bio, Seongnam, South Korea), and 100 bp DNA ladder (DYNE Bio) were employed for gel electrophoresis of PCR products.

#### 2.2. Determination of spin-coating conditions for PDMS membranes

The membrane fabrication process was adapted from previously reported spin-coating methods using Petri dishes [72,73]. Briefly, the PDMS pre-polymer base (part A) was mixed with the curing agent (part B) at a 10:1 ratio for 15 min. Bubbles formed during mixing were removed in a vacuum desiccator (NOVUS type, Duran, Mainz, Germany) for 20 min. A 10-cm-diameter PS Petri dish was inverted and mounted on a vacuum chuck of a spin coater (SC-100RPM, Rhabdos, Seoul, South Korea) as illustrated in Fig. S1 of Supplementary Information (S1). Once vacuum suction was engaged with the dish, a designated mass of PDMS (ranging from 2.2 to 6.6 g) was dispensed at its center. The dish was then rotated at various speeds ( $\omega = 500-7000$  rpm) and durations (t = 20-2400 s) for spin coating. After coating, the PDMS was cured in a preheated oven (Bio Konvision, Gwacheon, South Korea) at 80 °C for 30 min.

We aimed to investigate the relationship between spin-coating parameters and the resulting membrane thickness h. A particular focus was placed on achieving submicron-thick ( $<1~\mu m$ ) membranes without the use of toxic organic solvents such as hexane [74,75] and 3-butyl alcohol [76], by optimizing spin-coating conditions alone. Additionally, we sought to detach the membrane reliably without relying on sacrificial layers, including photoresist [74,77], water-soluble polyacrylic acid [78], polyvinyl alcohol [79], and gelatin [69], or adhesion-reduction coatings including Teflon and Parylene C [80], which can complicate the fabrication process.

After curing was completed, the membrane thickness was measured using a laser-scanning surface profilometer (VK-X3000, Keyence, Osaka, Japan). A step edge was created by removing a small section of the cured PDMS film from the dish with a scalpel (X-acto, Westerville, OH, United States). Thickness measurements were performed by scanning across this step edge.

# $2.3. \ \ Fabrication\ process\ of\ PDMS\ microballoon\ oscillators$

PDMS microballoon oscillators were fabricated using a membranetransfer method adapted from previous studies [72,73]:

Step 1. Two types of oscillator bodies were designed using Solid-Works CAD software (Dassault Systèmes, Vélizy-Villacoublay, France). The first design was for optimizing operating parameters for effective and robust acoustofluidic streaming (Fig. 2a). The device features a 2mm-diameter hole (or aperture) that defines the balloon diameter on a 1-mm thickness and 10-mm diameter circular base, along with an embedded Luer port (the design imported from GrabCAD [81]), to enable rapid pneumatic connection and disconnection. The second design (Fig. 2b) was tailored for DNA extraction applications. It retained the same-sized hole and Luer port but included a fused 20-mm-diameter circular base to which a PZT actuator was attached for acoustic excitation. Additionally, a cylindrical reaction chamber (8-mm tall, 5.85-mm inner diameter, total volume 215 µl) was fabricated and bonded atop the base to serve as a container for DNA extraction. Both oscillator types were fabricated using a high-resolution DLP 3D printer (Max X27, Asiga) with PlasClear resin. After printing, residual resin was thoroughly washed by immersing the printed parts in an isopropyl alcohol (IPA)-filled beaker and placing it in an ultrasonic bath (UC-20, Jeio Tech, Daejeon, South Korea). Post-printing curing was completed by UV for 30 min using a UV irradiator (Flash Cure Box, Asiga). Residual monomers and photoinitiators can inhibit PDMS curing [82,83]. To address this issue, the printed components underwent thorough cleaning with IPA and heat treatment inside an oven (3 h at 80 °C) to eliminate any

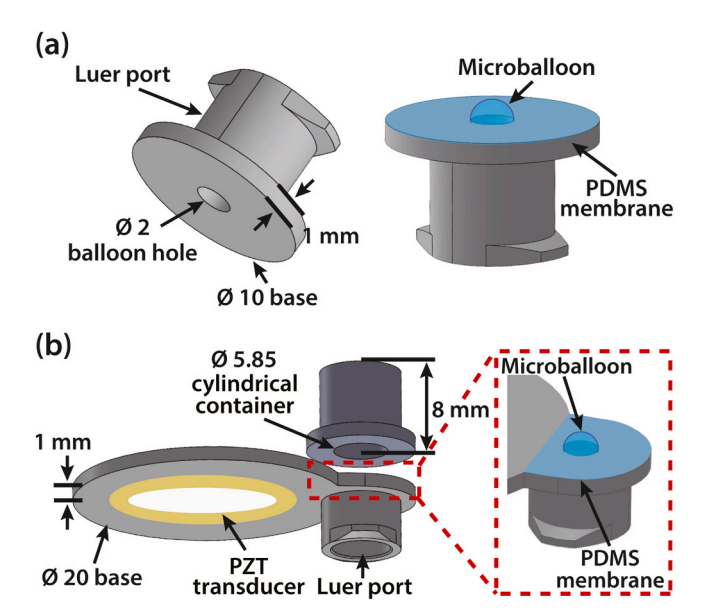


**Fig. 2.** Designs of microballoon oscillator bodies. (a) First type, used for optimizing operating conditions, features a 2-mm-diameter hole and a built-in Luer port for delivering pneumatic pressure to inflate the attached PDMS membrane. (b) Second type, designed for DNA extraction, includes a 20-mm-diameter base for attaching a PZT actuator. A fused 4-mm-diameter secondary base incorporates a Luer port for inflation, and a 3D-printed cylinder is bonded atop the base to form a reaction container.

curing inhibitors prior to PDMS-membrane bonding. Care was taken to avoid overheating, which could induce thermal-stress-induced cracks in the printed structures.

**Step 2.** A desired mass of uncured PDMS was spin-coated onto an inverted Petri dish, as described in Section 2.2. Specifically, 2.2 g of PDMS (10:1 ratio) was dispensed at the dish center (Fig. 3a). Membrane thickness was controlled by adjusting the spin speed  $\omega$  and time t (Fig. 3b). For example, 3000 rpm and 25 s yielded a  $\sim$ 32- $\mu$ m-thick membrane. After coating, the PDMS was thermally cured in an oven at 80 °C for 3 h (Fig. 3c).

Step 3. To bond the 3D-printed oscillator body to the cured membrane, a thin layer of PDMS (the same 10:1 ratio) was spin-coated directly onto the membrane as an adhesive layer (Fig. 3d). For example, 6000 rpm and 90 s yielded an  $\sim$ 8- $\mu$ m-thick adhesive film after curing. The 3D-printed body was then positioned with its circular base facing down onto the adhesive-coated membrane (Fig. 3e). The assembly was cured at 80 °C for 10 h (Fig. 3f). During curing, a gentle weight ( $\sim$ 7 g steel bolt) was applied to enhance adhesion. After curing, a permanent bond was established between the PDMS membrane and the 3D-printed body.

**Step 4.** The bonded oscillator was detached from the Petri dish by cutting the membrane around the circular base using a scalpel (X-Acto knife), as shown in Fig. 3g. This membrane-transfer approach leverages the weaker adhesion of PDMS to the PS surface compared to the 3D-printed acrylate resin [67]. Excess membrane extending beyond the base was trimmed to complete the device fabrication (Fig. 3h).

**Step 5.** For the second oscillator type (Fig. 2b), an additional step was required. A 3D-printed cylindrical chamber was aligned and bonded to the top surface of the circular base, where the PDMS membrane had been attached. Because the cylinder did not adhere to the PDMS surface, the membrane was trimmed to fit entirely within the cylinder's inner diameter, allowing secure bonding between the cylinder and the underlying base. This configuration enabled the chamber to contain cell and reagent solutions for lysis and DNA extraction without leakage.

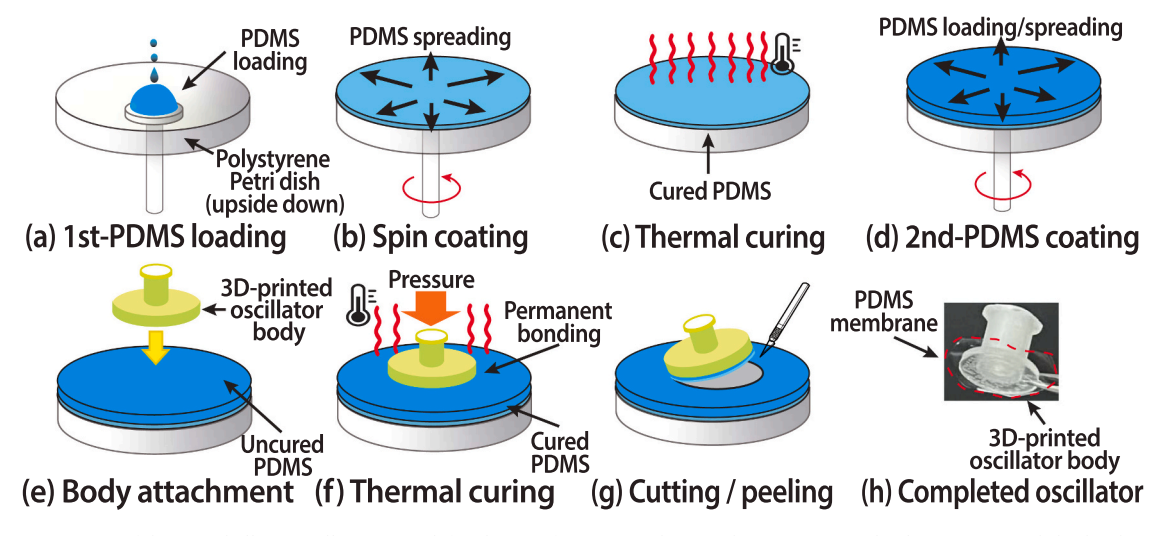
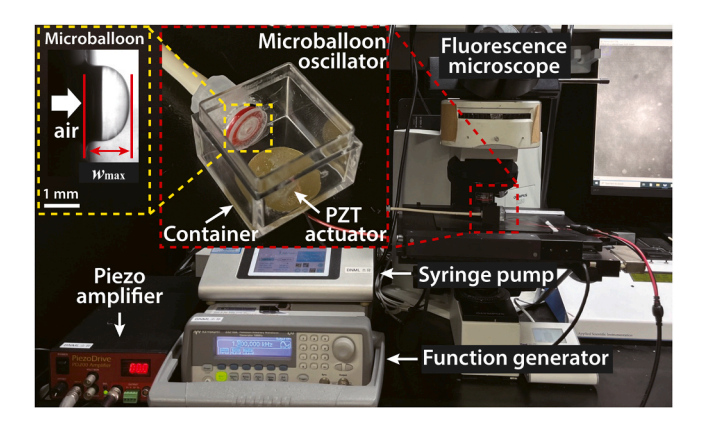


Fig. 3. Fabrication process of the microballoon oscillator. (a) A defined mass of PDMS was dispensed onto an inverted polystyrene Petri dish. (b) The PDMS was spin-coated at varying speeds and times to achieve a desired membrane thickness. (c) The membrane was thermally cured in an oven at 80 °C for 3 h. (d) A second, thinner PDMS layer was spin-coated onto the cured membrane to serve as an adhesive. (e) The 3D-printed oscillator body was gently placed onto the uncured adhesive layer with its base facing downward. (f) Permanent bonding between the PDMS membrane and oscillator body was achieved by curing the adhesive layer under a small weight ( $\sim$ 7 g) at 80 °C for 10 h. (g) The bonded assembly was separated from the dish by cutting the membrane around the circular base using a scalpel. (h) The fabrication was completed by trimming the excess membrane surrounding the base.

#### 2.4. Characterization of microballoon inflation and deflation

The microballoon was pneumatically inflated underwater using a syringe pump (Legato 100, KD Scientific, MA, United States) fitted with a 10-ml gas-tight syringe (#81620, Hamilton, Reno, NV, United States) as exhibited in Fig. 4.

The fabricated microballoon oscillator was mounted perpendicular to the microscope stage to capture inflation images using a rectangular PS container ( $25 \times 25 \times 11.7 \text{ mm}^3$ , Hoeaden, Guangdong, China). One side of the container was machined to have a 6-mm-diameter hole using a CO<sub>2</sub> laser cutter (Mini 24, Epilog, Golden, CO, United States). The oscillator was affixed to the container by inserting its male Luer port through the hole and sealing it with an O ring (inner diameter = 4.8 mm, Taekwang Special Rubber, Incheon, South Korea) and a female Luer connector. In this way, air leakage was minimized. The microballoon



**Fig. 4.** Custom setup for characterizing inflation/deflation and high-speed flow visualization. The PDMS microballoon oscillator was mounted horizontally onto a container (red inset). The microballoon was pneumatically inflated by injecting air through a syringe pump (yellow inset), while internal pressure was measured using an in-line pressure sensor (not shown). The balloon size  $w_{\rm max}$  was measured with calibrated bright-field microscopy. For flow visualization, the microballoon oscillator was excited using a PZT actuator bonded to the container bottom, which was driven by a function generator and a piezo amplifier. Resulting acoustic streaming images was captured using a high-speed fluorescence microscopy.

size  $w_{\rm max}$  (yellow inset) was measured from bright-field images acquired with an upright microscope (BX-50, Olympus, Tokyo, Japan) equipped with a high-speed sCMOS camera (Edge 5.5, PCO, Kelheim, Germany) and  $2 \times$  objective lens (Plan, Olympus). The captured images were calibrated with a microscope micrometer (Alpha Science, Seoul, Korea). Inflation pressure P was measured using an in-line pressure sensor (EIPS345, Fluigent, Le Kremlin-Bicêtre, France) to establish the inflation behavior, i.e., the relationship between  $w_{\rm max}$  and P.

Deflation behavior, expressed as  $w_{\text{max}}$  over time, was characterized using the same experimental setup with the in-line pressure sensor removed, as it was unnecessary for this measurement.

# 2.5. High-speed visualization of acoustic streaming

The operating parameters, including membrane thickness, excitation voltage, and balloon size, were experimentally optimized by examining the acoustic streaming generated around a vibrating microballoon. For streaming visualization, the same imaging setup (Fig. 4) was used, but in a fluorescence imaging mode. The high-speed sCMOS camera captured flow-field images at up to 100 frame per second (fps) at full resolution (2560  $\times$ 2160 pixels).

A PZT actuator (7BB-15–6L0, Murata, Kyoto, Japan) was bonded to the container bottom using instant glue (V-tech Strong Instant Adhesive, Youngil TS, Siheung, South Korea) to generate the acoustic field. The resonance frequency of the PZT actuator was  $6.0\pm1.0$  kHz according to the product specification. For clear imaging, the actuator's reflective brass surface was spray-painted white (Dupli-color, Motip Dupli, Hassmersheim, Germany) [29]. A suspension of fluorescence tracer microbeads (#FH-10052–2, 10–14  $\mu m$  diameter, Spherotech, Lake Forest, IL, United States) was loaded into the container, so that the inflated PDMS membrane (yellow inset) was exposed to the bead solution. During imaging, the container was left open to accommodate the short working distance of the objective lens ( $\sim\!5.8$  mm).

Resonance frequencies of our devices (typically 5.7–6.1 kHz) were determined using electromechanical impedance spectroscopy (EMIS) via an impedance analyzer (MFIA, Zurich Instruments, Zurich, Switzerland), as described in our previous work [29,32]. The PZT actuator was driven at resonance using a sinusoidal voltage signal ( $V_{\rm pp}$ ) generated by a function generator (33210 A, Keysight, Santa Rosa, CA, United States) and amplified with a piezo amplifier (20 × gain, PD200,

PiezoDrive, Newcastle, Australia). The container was filled with 2.5-ml of the bead suspension, yielding a fluid depth of  $\sim 5.12$  mm. The microballoon's position was 0.97-mm below from the water surface to enhance flow visualization by minimizing out-of-plane (Z-axis) components. High-speed images of fluorescence tracers were recorded at 100 fps for 2 s (200 frames total). Flow streamlines were synthesized from these images using ImageJ (NIH, Bethesda, MD, United States) and subsequently analyzed using the FlowTrace plugin.

# 2.6. Optimization of operating conditions

The operating parameters, i.e., membrane thickness (h), excitation voltage ( $V_{\rm exc}$ ), and balloon size ( $w_{\rm max}$ ), were systematically optimized for effective and reliable acoustic streaming. Performance was evaluated qualitatively by comparing flow streamlines. Key indicators are the spatial extent (coverage) and the length of individual streamlines (flow velocity). A series of experiments were conducted by independently varying the membrane thickness ( $10-100~\mu m$ ), excitation voltage ( $10-100~V_{\rm pp}$ ), and balloon size (0.06-1.5~mm). Optimal conditions were then determined by balancing acoustic-streaming strength with device stability. These optimized parameters were subsequently used for functional demonstrations, including ink mixing and DNA extraction.

# 2.7. Prediction of balloon size using finite element analysis

As the microballoon size  $w_{\rm max}$  is a critical factor in determining streaming performance, theoretical prediction of  $w_{\rm max}$  is desirable for rational micromixer design.  $w_{\rm max}$  depends on multiple parameters including the mechanical properties of PDMS, device geometry, and applied pressure. However, a simple linear model [84] fails to reflect the observed inflation behavior, showing unacceptable discrepancies (see Fig. S2 in SI). Therefore, an FEA (finite element analysis) method was employed.

Motivated by recent findings that soft materials fabricated by spin-coating, such as PDMS Sylgard 184, exhibit thickness-dependent mechanical properties [67,85] and given the challenges to directly measure the mechanical properties of ultrathin elastomeric membranes using conventional techniques (e.g., tensile test using a universal testing machine), the unknown mechanical properties of PDMS were investigated as a function of membrane thickness through FEA. Forward models were constructed using the finite element (FE) framework and inverse problems were solved to determine the best-fitting material parameters for each given thickness [86]. We used the nonlinear FE package ABAQUS (Dassault Systèmes) and adopted the Yeoh model as the constitutive model to describe the nearly incompressible hyperelastic behavior of ultrathin PDMS [87]. The Yeoh strain energy density function [88] *W* is defined as

$$W = \sum_{i=1}^{3} C_{i0} (\bar{I}_1 - 3)^i + \frac{1}{D_1} (J - 1)^2$$
 (1)

where  $\bar{I}_1$  is the distortional part of the first invariant of the right Cauchy-Green deformation tensor  $\mathbf{C} = \mathbf{F}^T \mathbf{F}$ , with the deformation gradient tensor  $\mathbf{F}$ , and J is the determinant of  $\mathbf{F}$ . The coefficients  $C_{10}$ ,  $C_{20}$ , and  $C_{30}$  present the material stiffnesses, and  $D_1$  is related to the inverse of the bulk modulus. The material was assumed to be nearly incompressible, with an initial Poisson's ratio of 0.4995 [89].

Three different membrane thicknesses, 10, 40, and 100  $\mu$ m, were considered for FE simulations. Each microballoon oscillator was modeled based on the corresponding experimental geometry, namely the aperture radius (i.e., hole radius) and membrane thickness (Fig. 5). The area defined by the aperture radius was free to deform under a uniform pressure P applied over the surface. Outside of this surface was constrained with all translational degrees of freedom to represent its permanent bonding to the oscillator body.

After mesh convergence tests, the FE model was constructed with

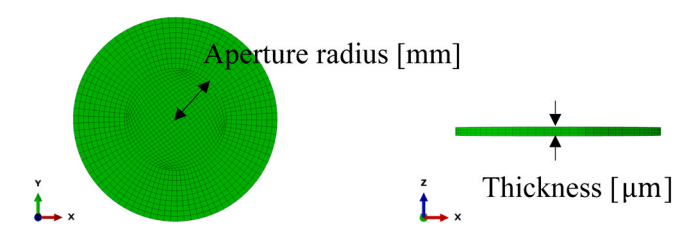


Fig. 5. Finite element model of a circular thin membrane defined by an aperture radius and membrane thickness.

6072 nodes and 4419 elements, using continuum hexahedral elements. By incrementally increasing pressure applied to the device, we measured deflected membrane heights (microballoon size  $w_{\rm max}$ ) to compare with experimental results. The maximum principal stress distribution was also analyzed to identify regions of potential membrane failure. Lastly, the pressures required to inflate microballoons of different aperture radii and thicknesses to target sizes were predicted using the model to provide guidelines for device design.

# 2.8. Mixing performance analysis

The mixing performance of the microballoon oscillator (first device type; Fig. 2a) was evaluated under bright-field imaging. Due to a limited field of view of the microscope (Fig. 4) for observing the entire mixing region, a separate imaging setup was constructed following a configuration similar to our previous work [29,32], as illustrated in Fig. S3 (SI).

Briefly, the mixing process was recorded using an sCMOS camera (CS2100M-USB, Thorlabs, Newton, NJ, United States) equipped with a  $1 \times \text{macro}$  lens (EF 50 mm f/2.5, Canon, Tokyo, Japan). The microdevice was mounted on a custom-built XY-translational stage. Illumination was provided by two LED light sources (LED-50W, AmScope, Irvine, CA, United States). A light diffuser (PULUZ, Shenzhen, China) was attached to the light-guide tips to reduce glare. The same function generator and piezo amplifier described in Section 2.5 were employed for excitation.

Due to challenges in using the excessive liquid volume in the PS container (12.5 ml) to characterize mixing, a smaller custom container with halved internal dimensions (16.4  $\times$  8.2  $\times$  11 mm  $^3$  per compartment) was fabricated using fused deposition modeling (FDM) 3D printer (X1, Bambu Lab, Shenzhen, China) and PLA filament (PLA Basic, Bamboo). Only one compartment, where the microballoon oscillator (inflated to  $\sim$ 0.8 mm) was mounted horizontally, was used for mixing experiments. A 6- $\mu$ l droplet of black ink was gently injected into a 600  $\mu$ l of DI water preloaded into the compartment. The PZT actuator attached to the container bottom was excited at the resonance frequency using 60  $V_{pp}$ . Bright-field images were captured at 30 fps for 200 s. A control experiment was conducted under identical conditions without excitation.

Grayscale image sequences were analyzed in ImageJ to extract pixelwise intensity values across the region of interest (ROI). The mixing index (MI) was calculated using the following expression [32]:

$$MI = 1 - \sqrt{\frac{1}{N} \sum_{i=1}^{N} \left(\frac{c_i - \overline{c}}{\overline{c}}\right)^2}$$
 (2)

where  $c_i$  is the intensity of ith pixel, and  $\overline{c}$  is the average intensity within the ROI. In this context, MI=  $\sim$ 0 corresponds to an unmixed state while MI=  $\sim$ 1 indicates a fully mixed state. Due to inherent imaging noise, MI typically plateaus below 1. The mixing time was defined as the point where MI reached 90 % of its steady-state value.

# 2.9. Cell lysis and DNA extraction using the microballoon oscillator

To demonstrate the practical utility of our microballoon oscillator,

we performed cell lysis and subsequent DNA extraction using the second device type (Fig. 2b), as exhibited in Fig. 6. The K562 human chronic myeloid leukemia cell line was used for this application.

Upon arrival, cells were centrifuged at 4000 rpm for 5 min using a centrifuge (5810 R, Eppendorf, Hamburg, Germany) to remove the frozen culture medium. Resulting cell pellets were resuspended in fresh RPMI-1640 culture medium. A 4-ml cell suspension ( $\sim$ 4.2  $\times$ 10<sup>6</sup> cells/ml) was prepared and stored at 4  $^{\circ}$ C until use. Cell concentration was measured using a hemocytometer (C-Chip, INCYTO, Cheonan, South Korea), and cell images were acquired with an inverted microscope (IX-73, Olympus) equipped with an sCMOS camera (Zyla 5.5, Andor Technology, Belfast, United Kingdom). Cell counting was performed using the Multi-point tool of ImageJ.

The experimental protocol was adapted from our previous cavitation-microstreaming-based DNA extraction workflow [29], with modifications to accommodate the different device geometry and fluid dynamics: specifically, an 8-mm-tall, 5.85-mm-inner-diameter cylindrical container (215- $\mu L$  volume) compared to the previously used 0.5-mm-thick flat microchamber (100  $\mu L$ ). In addition, PCR tape (#AB-0558, Thermo-Fisher, Waltham, MA, United States) was used for container sealing instead of Teflon tape. Conceptually, the procedure resembles conventional microtube-based DNA extraction using magnetic beads, with acoustofluidic mixing replacing vortexing. An experimental setup, similar to that used for mixing performance characterization, was employed to monitor the entire DNA extraction process (Fig. S4 in SI). The complete protocol is described in Section S.1 of SI. A summary is presented below:

**Step 1: Device preparation.** The oscillator device is securely mounted onto a custom 3D-printed jig fixed to the XY stage (Fig. S4 in SI) throughout all assay steps. The container is thoroughly cleaned using

 $1 \times PBS$  for 1 min for new devices or sequentially with 99.5 % ethanol and  $1 \times PBS$  for 1 min each for reused devices (Fig. 6a). All liquid handling was performed using a micropipette.

Step 2: Reagent/sample loading. A 40-µL solution of ethanol containing silica-coated magnetic beads is introduced into the container, followed by a 63-µL mixture of cells, lysis buffer, and Proteinase K (Fig. 6b). After loading, the container is sealed with PCR tape.

**Step 3: Cell lysis.** The reagents and cells are mixed for lysis using acoustic streaming generated by the microballoon oscillator located at the container bottom (Fig. 6c). Genomic DNA and cellular contents are released, with DNA selectively adsorbed to the silica-coated magnetic beads.

Step 4: Bead collection and removal of intracellular materials. A neodymium magnet is placed against the container wall to aggregate the suspended magnetic beads into a compact cluster (Fig. 6d). After the actuator is deactivated, the PCR tape is removed, and the supernatant is aspired to remove cellular debris.

Step 5: Purification. 100-µL of wash buffer I is added while retaining the DNA-bound magnetic beads on the wall. After resealing the container, the magnet is removed to resuspend the beads. Acoustic mixing is activated to wash residual impurities from the beads while the DNA remains bound (Fig. 6e). After mixing, beads are recollected magnetically, the tape is removed, and the wash solution is discarded (Fig. 6f). This step is repeated using wash buffer II.

Step 6. DNA elution. 100  $\mu$ L of elution buffer is added to the container holding the DNA-bound beads. After resealing, the magnet is displaced to resuspend the beads. The microballoon is excited to release DNA from the bead surface (Fig. 6g). After mixing, the empty beads are magnetically recollected. The tape is removed, and the eluted DNA solution is collected for downstream analysis (Fig. 6h).

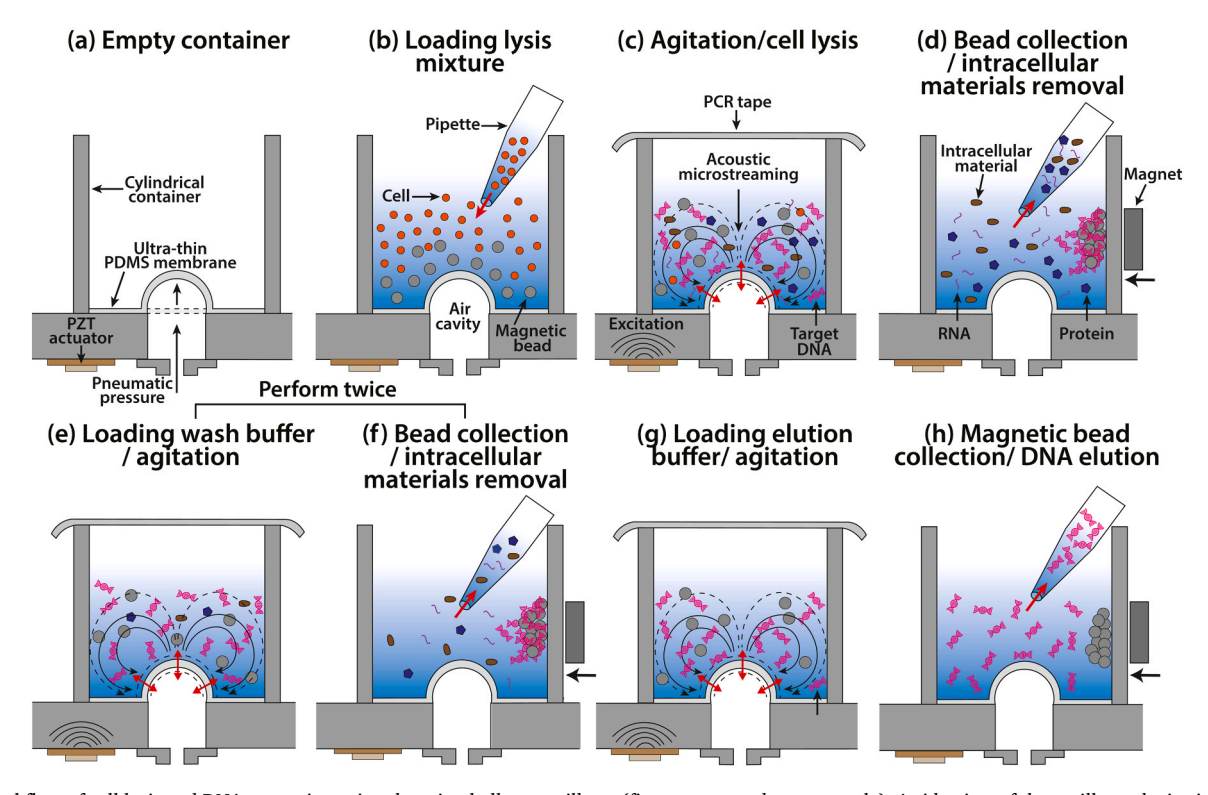


Fig. 6. Workflow of cell lysis and DNA extraction using the microballoon oscillator (figures are not drawn to scale). A side view of the oscillator device is illustrated for each step. Step 1. (a) The cylindrical container is thoroughly cleaned prior to use. Step 2. (b) Silica-coated magnetic beads in ethanol are loaded, followed by a solution containing cells, lysis buffer, and Proteinase K. Step 3. (c) The device is excited at its resonance frequency via the bonded PZT actuator, generating acoustic streaming from the bottom. As cells lyse, intracellular contents are released, and DNA is adsorbed to the beads. Step 4. (d) After the actuator is turned off, a permanent magnet is applied to the container wall to collect the beads. The supernatant containing unwanted cellular debris is discarded. Step 5. (e) A first wash buffer is introduced, and the device is re-excited. (f) DNA-bound beads are collected magnetically, and the wash solution containing residual impurities is discarded. (e) and (f) are repeated with a second wash buffer. Step 6. (g) Elution buffer is introduced, and the device is re-excited, releasing DNA from the beads. (h) Beads are recollected, and the DNA solution is retrieved for downstream applications.

#### 2.10. Cell lysis and DNA extraction using a commercial kit

As a control, DNA extraction was performed using the MagaZorb DNA Mini-Prep Kit, a commercially available magnetic-bead-based extraction kit. The procedure followed the same protocol described in our previous study [29]. The complete protocol is reproduced in Section S.2 of SI.

# 2.11. Performance analysis of DNA extraction

To evaluate the performance of our microballoon-based DNA extraction method, both DNA concentration and purity were quantified using a UV/Vis spectrophotometer (NanoPhotometer-P330, Implen, Bayern, Germany). The results were benchmarked against those obtained using the commercial kit.

DNA concentration was determined by measuring UV absorbance at 260 nm (A260), with background correction at 320 nm (A320). DNA purity was assessed based on the A260/A280 and A260/A320 absorbance ratios. Further details regarding the measurement protocol and data interpretation can be found in our previous publication [29].

#### 2.12. PCR and gel electrophoresis

To evaluate the quality of DNA extracted using our device compared to that obtained with the commercial kit, PCR (polymerase chain reaction) and agarose gel electrophoresis were performed. A 116-bp von-Willebrand-factor (vWF) gene was amplified using a specific primer set and a thermocycler (#TC9639, Benchmark Scientific, Sayreville, NJ, United States).

Each 20-µL PCR reaction mixture comprising 1 µL of forward primer and 1 µL of backward primer (final concentration of 0.0125 mM each), 10 µL of 2  $\times$  DNA free-HotTaq PCR Master Mix, 3 µL of DNA sample, and 5 µL of nuclease-free DI water was loaded into a 0.2-ml PCR tube (PCR-02-C, Axygen, Corning, NY, United States) for thermocycling. The amplification cycle consists of a denaturation step at 95 °C for 5 min, followed by annealing at 55 °C for 30 s, and extension at 72 °C for 1 min. The subsequent 35 cycles followed the same protocol, except that each denaturation step was shortened to 1 min. A final extension step was performed at 72 °C for 5 min. The following primer sequences were used for amplification [29]:

Forward primer: 5'-TCAGTATGTGACTTGGATTG-3'

Backward primer: 5'-GATAAATACATAGGATGGATGG-3'.

PCR products, stained with Dyne LoadingSTAR dye, were analyzed via electrophoresis on 2 % w/v agarose gel at 230 V for 70 min. DNA bands were visualized using a gel scanner (Dux GelDoc, Biomedux, Suwon, South Korea). Additional procedural details are available in Section S.3 in SI.

#### 3. Results and discussion

# 3.1. Optimizing spin-coating conditions for minimizing PDMS-membrane thickness

The thickness of a spin-coated film, h, is empirically related to the rotational speed  $\omega$  according to the following model [84]:

$$h = k\omega^{\alpha} \tag{3}$$

where k and  $\alpha$  are experimentally derived constants. k is related to viscosity and  $\alpha$  is typically negative, indicating an inverse relationship between h and  $\omega$ . To establish a baseline behavior, 2.2 g of PDMS was loaded and spin-coated for 20 s at varying rotational speeds. The resulting membrane thicknesses were curve-fitted to Eq. (3) using Sigmaplot 14.0 (SYSTAT, Chicago, IL, United States) as shown in Fig. 7a. The data yielded fitted parameters  $k=15822~\mu m$  and  $\alpha=-0.77$ . The minimum thickness achieved under these conditions was 11.9  $\mu m$  at

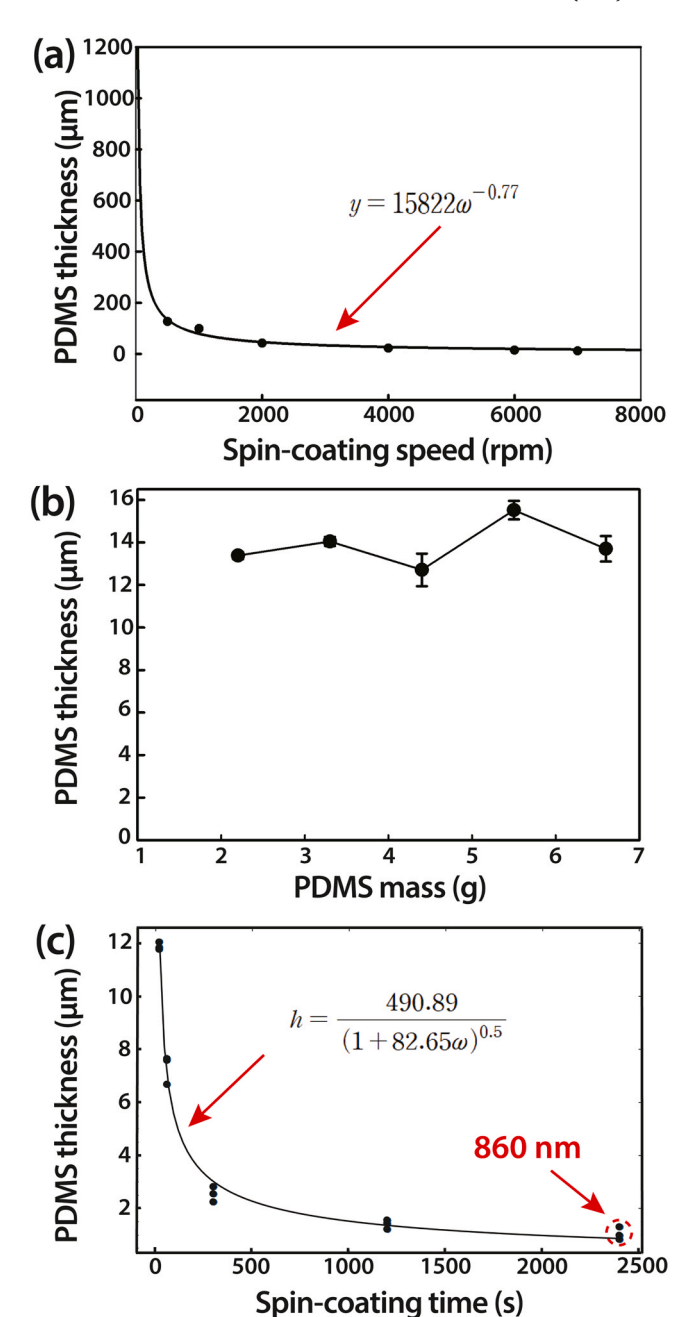


**Fig. 7.** Optimization of spin-coating conditions for fabricating ultrathin PDMS membranes without solvent dilution. (a) Membrane thickness h as a function of spin-coating speed  $\omega$  at a fixed PDMS mass of 2.2 g and coating time of 20 s. (b) Effect of varying PDMS mass (2.2-6.6 g) on membrane thickness at 7000 rpm and 20 s, and (c) membrane thickness h as a function of spin-coating time t at a constant speed of 7000 rpm and mass of 2.2 g. Submicron thickness (860 nm) was achieved only by extending the coating time, demonstrating solvent-free membrane fabrication.

7000 rpm, insufficient for sub-µm-scale films.

Next, we investigated the effect of increasing the PDMS mass (2.2-6.6 g) at constant spin speed (7000 rpm) and coating time (20 s). As shown in Fig. 7b, no substantial change in h was observed, consistent with previous findings [90]. To achieve thinner membranes, the spin-coating time t was extended (500-2400 s) while keeping the PDMS mass (2.2 g) and spin speed (7000 rpm) constant. This dataset was fitted to an extended empirical model that accounts for spin time [91]:

$$h = \frac{h_0}{(1 + c\omega^2 h_0^2 t)^{0.5}} \tag{4}$$

where c and  $h_0$  are fitting parameters. Curve fitting yielded parameters  $h_0 = 490.89 \, \mu \text{m}$  and  $c = 7.0 \times 10^{-10} \, \text{rpm}^{-2} \, \mu \text{m}^{-2} \, \text{s}^{-1}$ , as shown in Fig. 7c. By increasing t to 2400 s, we achieved a membrane thickness of 860 nm, successfully entering the sub- $\mu$ m regime.

To the best of our knowledge, this is *the first report* of sub-µm membranes fabricated from standard Sylgard-184 PDMS without using toxic organic solvents. Producing membranes thinner than 10 µm typically requires dilution with solvent such as hexane or 3-butyl alcohol [67,80, 92,93]. An exception is sub-µm membranes fabricated using Sylgard 527, a lower-viscosity variant [73]. Our approach thus provides a cleaner and more accessible alternative for ultrathin PDMS membrane fabrication.

In the current study, membranes with thicknesses ranging from 10 to  $100~\mu m$  were employed for constructing microballoon-based micromixers. Sub-micrometer membranes, though successfully fabricated, were deemed too fragile for the present micromixer configuration, having a relatively large pneumatic hole (2-mm diameter). However, we envision their application in future designs, further miniaturized with smaller holes (say, hundreds of micrometers or less), where thinner membranes could be more reliably accommodated.

#### 3.2. Characterization of microballoon inflation

Microballoons were inflated using a syringe pump at a flow rate of 5 ml/min for 35 s. The membrane deflection  $w_{\rm max}$  was measured as a function of applied pressure using an in-line pressure sensor. All measurements were conducted under water at a depth of 0.97 mm, where the hydrostatic pressure was negligible (~50 Pa). The resulting deflections for the three membrane thicknesses are plotted in Fig. 8. Experimental data were curve-fitted using a five-parameter exponential function  $y=y_0+a$  exp(-bx)+c exp(-dx) using Sigmaplot, yielding excellent fits with  $R^2=0.994$ , 0.999, and 0.999 for 100-, 40-, and 10- $\mu$ m microballoons, respectively. As expected, thinner membranes exhibited greater deflection under a given pressure due to their higher compliance.

# 3.3. Characterization of the microballoon deflation and lifetime

PDMS is practically impermeable to water [94], but permeable to

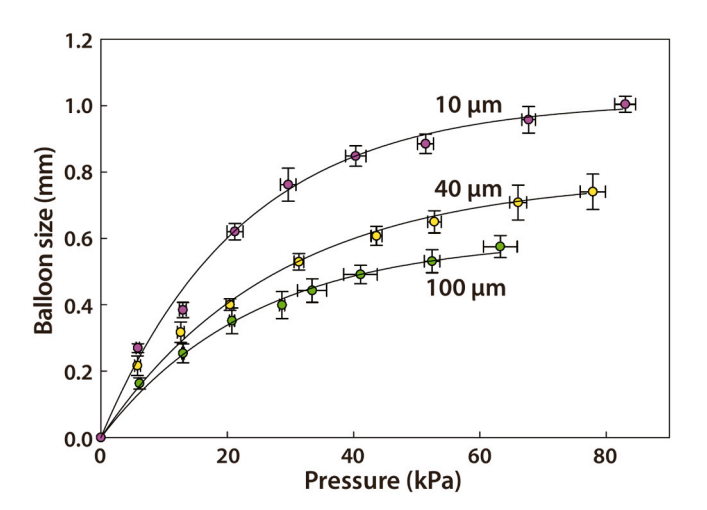


**Fig. 8.** Inflation characteristics of PDMS microballoons with membrane thicknesses of 10, 40, and 100  $\mu$ m measured underwater as a function of applied pressure. Data represent  $w_{\rm max}$ , deflection at the membrane center (n=3 for each thickness). The relationship illustrates thickness-dependent compliance, with thinner membranes exhibiting larger deflections under identical pressures.

gases [95]. For example, the gas permeability of oxygen, hydrogen, and nitrogen at 35°C is 52531, 58440, and 26266 cm³·mm/m²·day·atm, respectively [96]. In contrast, Parylene C, commonly used stiffer membrane material, has a significantly lower oxygen permeability of 2.83 cm³·mm/m²·day·atm [97]. Consequently, PDMS-based microballoons are expected to deflate gradually due to air permeation, leading to a decline in acoustic streaming. Therefore, it is important to characterize the time-dependent reduction in microballoon size  $w_{\rm max}$  to estimate operational lifetime.

To investigate deflation behavior, microballoons with thicknesses of 10, 40, and 100  $\mu$ m were inflated to an equal initial size and allowed to deflate over time for direct comparison. During preliminary tests, microballoons ruptured prematurely if inflated at 5 ml/min (as used in Section 3.2). The absence of the pressure sensor, which acted as a pneumatic resistor, likely caused unregulated airflow surges and membrane failure. To prevent this, the flow rate for the initial inflation was reduced to 1 ml/min for all subsequent experiments. We unexpectedly noted that thicker membranes ruptured at smaller balloon sizes than thinner ones during initial inflation. For instance, the smallest ruptured balloon size was 0.68 mm (average = 0.70 mm, n = 3) for the 100- $\mu$ m membrane, whereas no ruptures occurred for thinner membranes at the same size. Consequently, an initial target balloon size of 0.6 mm (actual average = 0.59 mm) was adopted as a safe limit for all thicknesses.

The deflating balloon size was recorded over time as shown in Fig. 9. The data were fitted using a five-parameter exponential decay model  $y = y0 + a \cdot \exp(-bx) + c \cdot \exp(-dx)$  using Sigmaplot. The fits achieved excellent agreement ( $R^2$ = 0.999, 0.999, and 0.997 for 100-, 40-, and 10μm membranes, respectively). As expected, thinner membranes deflated more rapidly due to higher air permeability. Within the first 30 min, the 10-µm membrane exhibited the largest size reduction (45 %), while the 100-µm membrane showed the smallest (23.7 %). After this initial phase, the rate of deflation decreased for all cases, while the relative order of deflation remained the same for the 9-hour period. Interestingly, all three balloon types converged to a similar final size ( $\sim$ 0.20 mm) after 12 h, with total reductions of 67.8 %, 63.8 %, and 66.1 % for the 10-, 40-, and 100-µm membranes, respectively. The reason for this convergence is not fully understood, but it is likely that the driving force for air permeation, the pressure gradient across the membrane, decreases while approaching the steady state, because the internal pressure drops during deflation [98,99], slowing further air loss regardless of membrane thickness.

The operational lifetime, defined as the time to reach 90 % of the total size reduction based on fitted curves, was 4 h 27 min, 8 h 52 min,

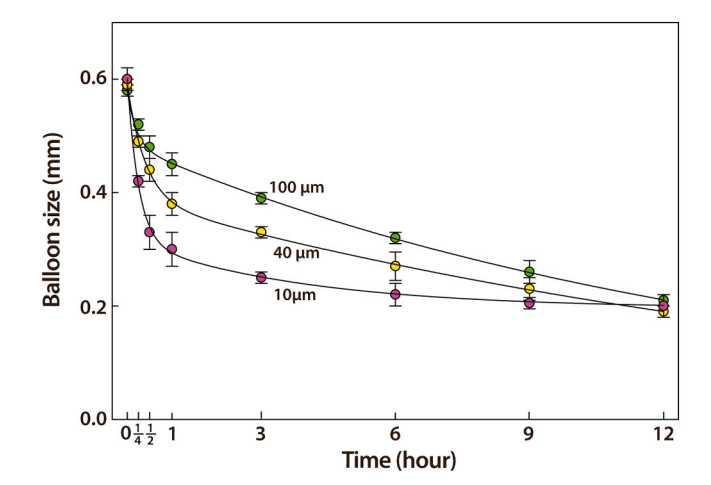


**Fig. 9.** Characterization of microballoon deflation via air permeation through PDMS membranes. The microballoon size  $w_{\rm max}$  was monitored underwater over time for different membrane thicknesses of 10, 40, and 100  $\mu$ m. Thinner membranes exhibited faster deflation, while all converged to a similar final size after 12 h.

and 9 h 59 min for 10-, 40-, and 100-um membranes, respectively.

# 3.4. Optimization of operating conditions based on streaming analyses

To determine optimal operating conditions, we investigated the effects of membrane thickness (h), excitation voltage ( $V_{\rm exc}$ ), and balloon size ( $w_{\rm max}$ ) on acoustic microstreaming generated by oscillating PDMS microballoons. Cavitation microstreaming generates flows via viscous dissipation of acoustic energy at the vibrating air-liquid interface of entrapped bubbles [43,46]. Given this mechanism, we hypothesized that an oscillating ultrathin PDMS microballoon (i.e., a flexible membrane suspended over a cavity) could generate streaming with improved stability [47–49]. Indeed, membrane oscillation produced two counter-rotating vortices (Fig. 10), resembling those observed in cavitation microstreaming [29,32].

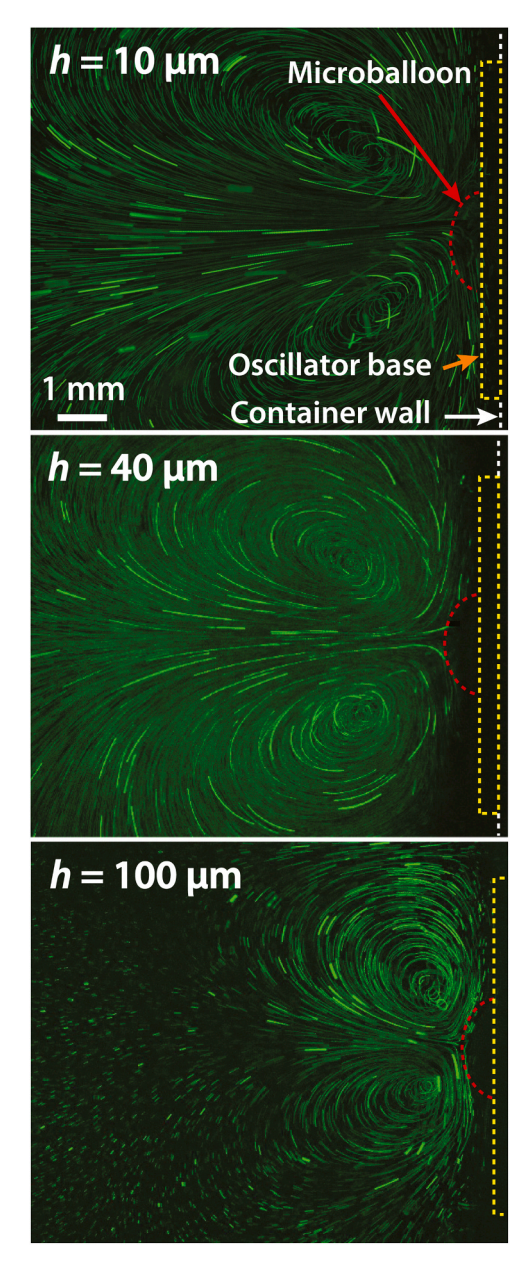


Fig. 10. Streamline images generated by PDMS microballoons with membrane thicknesses of 10, 40, and 100  $\mu m$ . Thinner membranes produced faster and broader streaming flows, as indicated by longer particle streaks and wider pathlines. For all cases, the balloon size  $(w_{max})$  was maintained at  $\sim\!0.55$  mm, and the excitation voltage  $(V_{exc})$  was 60  $V_{pp}$ .

#### 3.4.1. Determination of excitation frequency

For streaming analysis, we excited the PZT actuator at the resonance frequency of the fully assembled device (red inset of Fig. 4), which is a complex coupled mechanical resonator comprising the piezo actuator, polystyrene rectangular container, 3D-printed oscillator body, and inflated PDMS membrane. As previously reported, efficient elastic-wave propagation to the target resonator and surrounding fluid requires proper frequency matching between the target resonator (i.e., inflated membrane) and the overall structure [100,101]. Ideally, the entire coupled system should resonate at these or near the matched frequencies to maximize energy transfer. However, matching the low resonance frequency of our device (5.7-6.1 kHz) and the high resonance frequencies of ultrathin, inflated membranes (>20 kHz) is challenging in practice due to a large frequency difference. The resonance frequency of the polymer-based device was relatively small due to low acoustic impedance, high damping, and relatively large structural mass. A significant frequency mismatch between coupled components can lead to less effective wave propagation and reduced vibration amplitude [100]. Hence, exciting the system at the eigenfrequencies of the isolated (uncoupled) membrane (>20 kHz) can be suboptimal for our design. In contrast, exciting the PZT actuator at the resonance frequency of the entire device, where the overall mechanical vibration is maximized, can yield more effective acoustic streaming. Additionally, the affordable piezoelectric actuator used here is designed to operate in a low-frequency bending mode (6.0 kHz  $\pm$  1.0 kHz), rather than in thickness modes required for high-frequency operation. As a result, the actuator is more efficient when driven near its specified resonance (i.e., the coupled resonance frequency of our device), rather than at uncoupled microballoon eigenfrequencies (>20 kHz), further justifying excitation at the resonance frequency of the entire device.

To validate this approach, we compared the acoustic streaming performance at both the measured resonance frequency of the coupled system ( $\sim$ 6.1 kHz) and the 1st, 2nd, and 3rd eigenfrequencies of the isolated microballoon (22.446, 31.347 and 49.919 kHz, respectively, obtained via finite element modal analysis in Section 2.7) with the same excitation voltage of 10 Vpp. As shown in Fig. S5, the strongest streaming occurred at 6.1 kHz, followed by 22.2 kHz (likely due to small deviations between modeled and actual system behavior). Moreover, practically no acoustic streaming was observed at 31.3 and 49.9 kHz. These findings are consistent with our previous studies on cavitation microstreaming, where excitation at the chip-resonance frequency led to stronger streaming than excitation at the resonance frequency of an isolated bubble [29,32].

# 3.4.2. Optimization of membrane thickness

We then optimized membrane thicknesses by testing h=10, 40, and 100  $\mu$ m while maintaining constant balloon size (0.55 mm) and excitation voltage (60 V<sub>pp</sub>). Actual balloon sizes deviated slightly from the target due to the difficulty of precisely controlling inflation volume (e.g., = ~0.5 ml for  $w_{\rm max}=0.55$  mm). We assumed that the flexible PDMS membrane would generate strong acoustic streaming, considering the low Young's modulus of PDMS (12 kPa - 2.50 MPa), especially when compared to 5-to-7 orders-of-magnitude stiffer materials used in previous diaphragm-based streaming studies, such as thermoplastics (55–420 GPa), LPCVD silicon nitride (270 GPa), single-crystal silicon (130–188 GPa), and brass (102 GPa).

As exhibited in Fig. 10, streaming behavior followed consistent trends; thinner membranes produced both faster (evidenced by longer fluorescent-particle streaks) and broader flow fields (larger elliptical pathlines formed by counter-rotating flows). Among the tested conditions, the thickest membrane ( $h=100\,\mu\mathrm{m}$ ) generated the weakest streaming. While the 10- $\mu\mathrm{m}$  membrane produced the strongest streaming, it suffered from a significantly shorter operational lifetime (4 h 27 min) as shown in Section 3.3. Balancing streaming performance with durability,  $h=40\,\mu\mathrm{m}$  was selected as the optimal membrane thickness, achieving robust streaming while maintaining a functional lifetime

exceeding 6 h. For applications requiring short-term operation (say, <4.5 h), the 10- $\mu$ m membrane may be preferable due to its superior streaming intensity.

# 3.4.3. Optimization of excitation voltage

With membrane thickness fixed at the optimal value of  $h=40~\mu m$ , we investigated the effect of excitation voltage  $V_{\rm exc}$  on streaming performance over a range of 10–80  $V_{\rm pp}$ . Voltages above 80  $V_{\rm pp}$  were excluded due to the risk of premature PZT-actuator malfunction due to overheating. The balloon size  $(w_{\rm max})$  was maintained at 0.55 mm for all tests.

As shown in Fig. 11, the least effective streaming was observed at  $10~V_{pp},$  as expected. Both the velocity and spatial extent of acoustic microstreaming increased with rising voltage. However, at  $80~V_{pp},$  the formation of a drifting secondary flow, possibly streaming originating from the vibrating container walls, interfered with and partially suppressed the microballoon-induced streaming. Based on these observations,  $60~V_{pp}$  was determined as the optimal excitation voltage, providing strong and stable streaming without undesirable secondary-flow effects. Similar voltage-dependent trends were observed for devices fabricated with both thinner (10  $\mu m$ ) and thicker (100  $\mu m$ ) membranes (see Fig. S6 in SI).

# 3.4.4. Analysis of the impact of microballoon size on streaming

We next investigated the impact of balloon size ( $w_{max}$ ) on acoustic streaming. A larger balloon is expected to produce a broader oscillating membrane surface, thereby generating more extensive streaming regions. Additionally, due to the Poisson effect, inflation-induced thinning of the PDMS membrane can enhance streaming, consistent with the membrane thickness trends observed in Section 3.4.2. Care must be taken not to inflate the membrane beyond its limit, as excessive internal pressure can rupture the membrane (see Fig. S7 in SI) or cause rapid deflation after excitation, possibly due to undetected microtears.

To establish safe operating limits, we first determined the maximum

 $w_{\rm max}$  for each membrane thickness. For the 40-µm membrane, microballoons ruptured at an average size of 1.05 mm (n = 3), being a practical upper limit for inflation. For the 10- and 100-µm membranes, average rupture sizes were 1.47 and 0.7 mm, respectively (n = 3). Experimental observations for the 40-µm-thick microballoon confirmed that both streaming velocity and spatial coverage improved with increasing balloon size (Fig. 12). To validate the importance of membrane inflation, we also conducted a control experiment in which the syringe pump was disconnected, for no deliberate balloon expansion. In this case, the PDMS membrane remained essentially flat, with a slight deformation ( $w_{\text{max}} = 0.06 \text{ mm}$ ), possibly due to minor stretching caused by detachment from the Petri dish. Under this configuration, negligible acoustic streaming was observed, signifying the critical role of balloon inflation in generating effective acoustic streaming. To further evaluate the influence of membrane thickness on streaming behavior, we systematically tested combinations of balloon sizes and membrane thicknesses. Results are tabulated in Fig. S8 (SI).

Combining these finding with those from Sections 3.4.2 and 3.4.3, we conclude that streaming performance improves with (1) thinner PDMS membranes, (2) higher excitation voltage, and (3) larger microballoon sizes, provided that the reliability requirements are met, including membrane integrity, operational lifetime, and avoidance of secondary-flow suppression and thermal damage.

# 3.4.5. Characterization of device lifetime and optimization of microballoon

We investigated the long-term operational stability of the PDMS microballoon oscillator. As discussed in Section 3.3, PDMS microballoons gradually deflate due to air permeation, eventually diminishing acoustic streaming owing to the size-dependent streaming performance observed in Section 3.4.4. Although the thinnest membrane with the largest balloon ( $h=10~\mu\text{m}, w_{\text{max}}=0.61~\text{mm}$ ) demonstrated the most vigorous streaming (Fig. S8 in SI), its rapid deflation underscored the importance of evaluating device lifetime. While Section 3.3

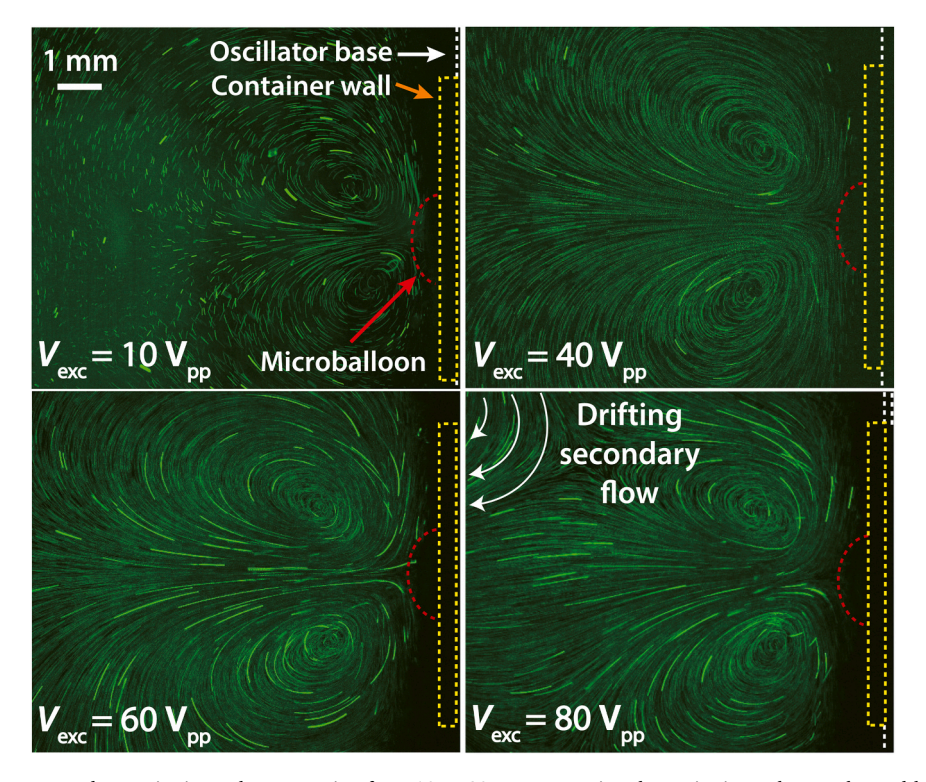


Fig. 11. Streamline images generated at excitation voltages ranging from 10 to 80  $V_{pp}$ . Increasing the excitation voltage enhanced both streaming velocity and spatial extent. At 80  $V_{pp}$ , however, the emergence of secondary flows, likely streaming induced from the vibrating container walls, disrupted the microballoon-driven streaming. Based on these results, 60  $V_{pp}$  was selected as the optimal excitation voltage. For all experiments, the balloon size ( $w_{max}$ ) was set was ~0.55 mm, and the membrane thickness (h) was 40 μm.

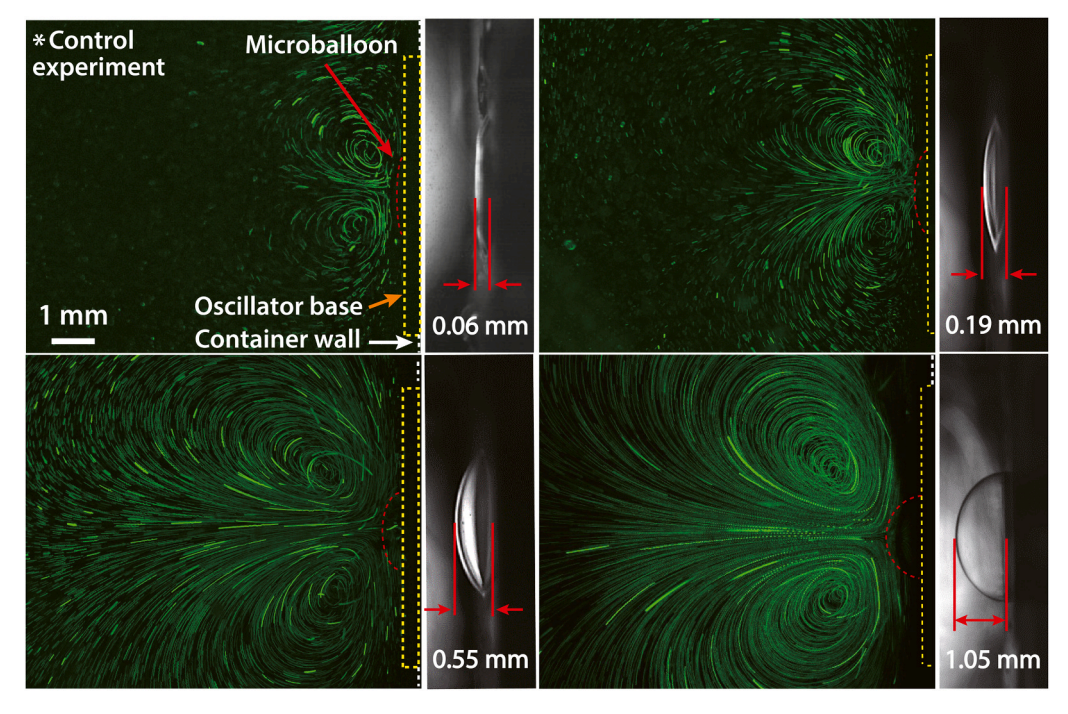


Fig. 12. Streamline images generated by PDMS microballoons with varying sizes ( $w_{max}$ ). Both flow speed and range increased with balloon size, indicating enhanced acoustic streaming performance. A control experiment with uninflated membrane ( $w_{max} = 0.06$  mm, likely due to membrane stretching caused by detachment from the Petri dish) exhibited negligible streaming. For all experiments, the membrane thickness was 40 μm, and the excitation voltage was 60 V<sub>pp</sub>.

characterized membrane shrinkage under static conditions without excitation, here we seek to evaluate device lifetime under active excitation at the optimized membrane thickness ( $h=40~\mu m$ ), focusing on the duration of sustained streaming performance.

A 40  $\mu$ m-thick microballoon, initially inflated to  $w_{max}=1.05$  mm, deflated to 0.21 mm over 24 h (80 % reduction, Fig. S9 in SI). Streamline analysis indicated that effective acoustic streaming persisted for 6 h (i.e., a 61 % size reduction) beyond the operational timescale of typical microfluidic assays. However, this large balloon size suffered from a low

manufacturing yield ( $\sim$ 60 %), with frequent ruptures or membrane delamination during inflation, even at a modest air-injection rate of 1 ml/min.

To address this problem, we repeated the experiment with a smaller balloon ( $w_{max} = 0.78$  mm; target = 0.8 mm) as exhibited in Fig. 13. The fabrication yield was 100 % because the size was ~26 % below the practical size limit of 1.05 mm for 40- $\mu$ m membranes. Similar to the case of  $w_{max} = 1.05$  mm (Fig. S9 in SI), this configuration also maintained effective streaming for 6 h despite a 67 % size reduction. Balancing

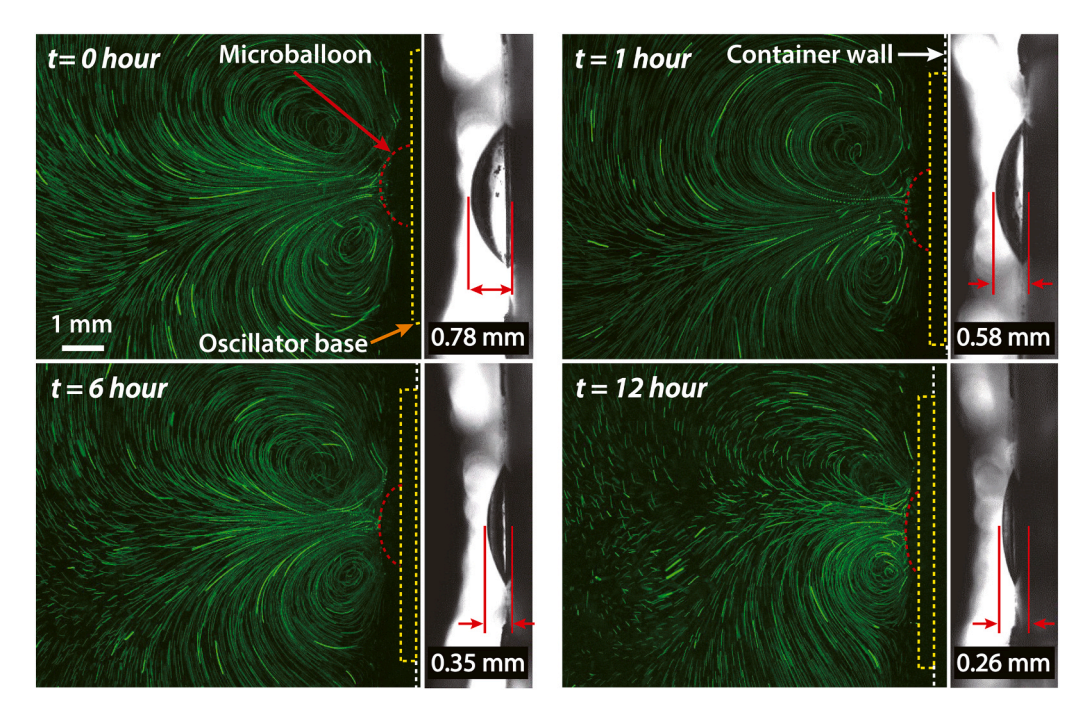


Fig. 13. Long-term stability test. The balloon gradually deflated from 0.78 mm to 0.26 mm (a 66 % reduction) over 12 h due to air permeation through the PDMS membrane. Despite the size decrease, strong streaming persists for over 6 h. The membrane thickness was 40  $\mu$ m, and the excitation voltage was 60  $V_{pp}$ .

fabrication yield, operational lifetime, and streaming performance, we identified  $w_{\rm max}=0.8$  mm as the optimal balloon size.

# 3.4.6. Optimized operating condition

By balancing the streaming speed and spatial coverage, long-term stability, and fabrication yield, the optimal operational condition was determined to be a 40- $\mu$ m-thick PDMS membrane with a balloon size of 0.80 mm, excited at 60 V<sub>pp</sub>. For microfluidic assays requiring shorter operational times (e.g., <1 h), microballoons with a 10- $\mu$ m-thick PDMS membrane may be preferable due to their superior mixing performance.

# 3.5. Prediction of microballoon size using a finite element model

For a small deflection, the theory of a clamped circular diaphragm under uniform pressure predicts  $w_{\text{max}}$ , the maximum deflection at the diaphragm center, as the following expression [102]:

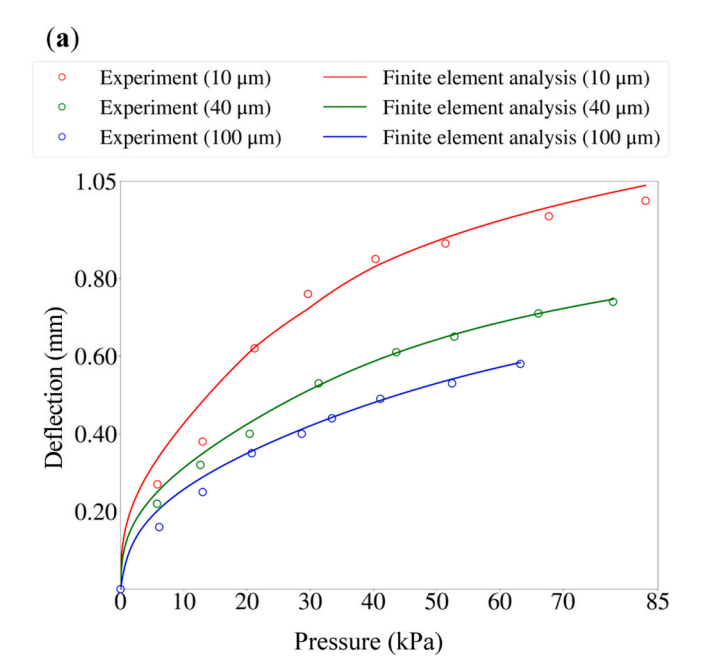
$$w_{\text{max}} = \frac{3(1 - v^2)R^4P}{16Eh^3} \tag{5}$$

where R is the diaphragm radius (or aperture radius), E is the Young's modulus, and v is the Poisson's ratio. According to this model,  $w_{\rm max}$  increases linearly with P within the small-deflection regime. For our microballoon device,  $R = 1 \times 10^{-3}$  m and v = 0.4995 [68,89].

Previous studies have reported that Young's modulus of a PDMS membrane depends on thickness [67,69,80] because spin coating induces shear stresses that align and stretch the random coil structure of polymer chains into a reordered, stronger network [67]. We estimated the Young's moduli by extrapolating and interpolating published data (see Fig. 3 in ref. [67]). We assumed negligible temperature dependence because curing temperatures were not specified in the referenced studies [68,103]. The estimated Young's moduli were  $E=1.11,\ 1.30,\$ and  $1.60\$ MPa for the membrane thickness  $h=10,\$ 40, and  $100\$ µm, respectively. However, the theoretical linear model (Eq. 5) deviated significantly from the experimental measurements across all thicknesses and pressure ranges (Fig. S2 in SI). This discrepancy became exacerbated for thinner membranes. To better capture the observed behavior, we performed finite-element (FE) simulations using the ABAQUS software package.

To explore the optimal parameter candidate for the Yeoh hyperelastic model, we utilized Latin hypercube sampling [104], with particle swarm optimization (PSO) [105,106]. Uniformly distributed parameters of the Yeoh model over a prescribed parameter range were sparsely sampled first, with each set enacting a particle in the PSO algorithm. The local and global best positions of the particles were then iteratively updated in a gradient-free manner to minimize the objective function, which was defined as the RMSE (root-mean-square error) between experimentally measured and simulated membrane heights ( $w_{\rm max}$ ) under applied pressure. The global best position was selected as the optimal parameter set after full iterations or under a convergence criterion that no further improvement in the RMSE is observed over a predefined number of additional cycles. The fitted material parameters of the Yeoh model are summarized in Table 1.

The FE simulation results using the optimized parameter set in Table 1 are shown in Fig. 14a, where the variation of membrane deflection  $(w_{\rm max})$  varies with respect to applied pressure. Deformed configurations with z-directional displacements are also presented in Fig. 14b, c, and d when the largest pressures in Figs. 14a, 83.03 kPa,



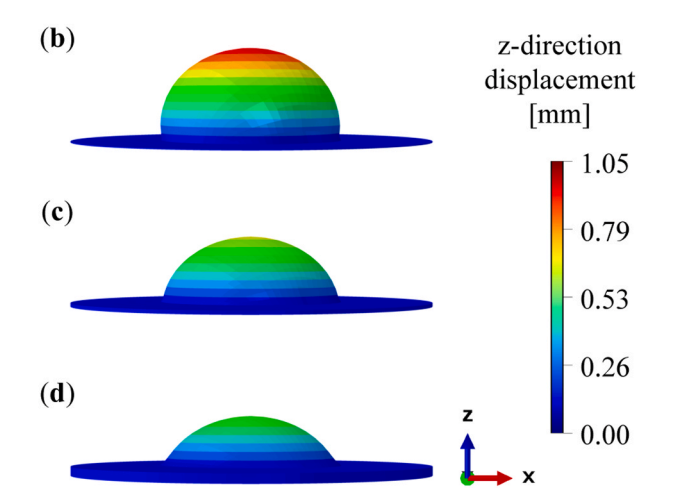


Fig. 14. Finite element simulation results. (a) Variation of deflection at the membrane centers ( $w_{max}$ ) with respect to applied pressure for membrane thicknesses of 10, 40, and 100  $\mu m$ . (b-d) Deformed configurations at maximum deflection with z-directional displacement obtained for membrane thicknesses of (b) 10  $\mu m$ , (c) 40  $\mu m$ , and (d) 100  $\mu m$ , respectively.

77.89 kPa, 63.24 kPa, respectively, are applied for each thickness. The model achieved excellent agreement with experimental data, yielding the coefficients of determination ( $R^2$ ) 0.980, 0.995, and 0.986 for membrane thickness of 10, 40, and 100  $\mu$ m, respectively. Furthermore, the predicted microballoon shapes closely matched experimentally observed shapes (data not shown), confirming the accuracy of the FE approach.

Overall deformation characteristics did not exhibit a clearly J-shaped nonlinearity in the pressure–deflection response of the ultrathin mem-

**Table 1**Constitutive model corresponding to each PDMS membrane thickness and their fitted material parameters obtained from finite element analysis.

Thickness (µm)		10	40	100
Yeoh strain energy density function coefficients	C <sub>10</sub> (kPa)	733.4	372.2	224.2
	$C_{20}$ (kPa)	39.83	0.689	1.135
	C <sub>30</sub> (kPa)	100.5	152.1	149.6
	$D_1$ (kPa <sup>-1</sup> )	$1.363 \times 10^{-6}$	$2.686 \times 10^{-6}$	$4.596 \times 10^{-6}$

brane [107], but rather showed a saturation behavior at higher pressures [108]. This saturation is likely due to the geometric constraints and boundary conditions imposed on the thin membrane, which limit further out-of-plane deformation at higher pressures.  $C_{10}$ , which corresponds to the linear term in the Yeoh model and primarily governs the initial stiffness, has the most significant influence on the deformation behavior observed in this experiment [88], whereas  $C_{20}$  and  $C_{30}$ , which account for higher-order nonlinearities, have comparatively smaller effects.

Using the identified hyperelastic material parameters for each membrane thickness and the given aperture radius, we further investigated the locations of maximum stress and the thinnest regions of the deformed membranes. The distribution of maximum principal stress for each thickness is shown in Fig. 15a, b, and c, respectively. To capture the stress evolution across different loading conditions, we performed simulations over ranges of applied pressures for the membrane thicknesses of 10, 40, and 100  $\mu$ m. The upper limit of the range is the pressure when the membrane rupture occurs for each thickness (see Section 3.4.4). The maximum principal stress profile at the apex location was calculated with respect to the applied pressure values for each membrane thickness (Fig. 15d). As expected, the maximum stress increased with increasing pressure and decreasing membrane thickness, which corresponded to a larger balloon size. The highest stress and thinnest region were observed near the top of the membrane after deformation. These results are consistent with our observations that ruptures frequently initiate at the inflated microballoon top, where the stress is highest and the membrane is thinnest (Fig. S7 is SI).

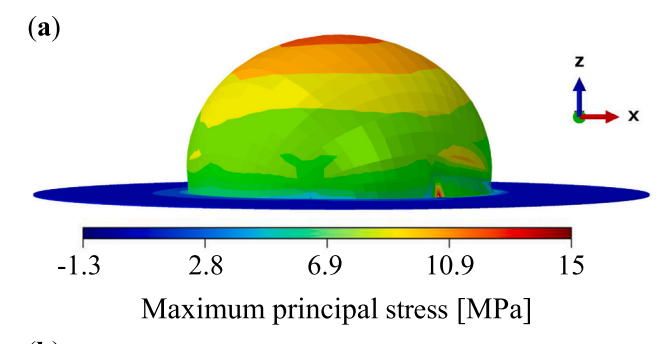
In addition, we investigated how the aperture radius affects the pressure required to reach the maximum attainable deflection for a given membrane thickness. Here, the maximum attainable deflection  $(d_{\rm max})$  is defined by the z-direction displacement when the maximum principal stress at the apex reaches the critical threshold value, which is the maximum stress as identified in Fig. 15d. In this context, we developed additional FE models with aperture radii of 0.5, 1, 1.5, and 2 mm. As examples, two representative displacement contours are shown in Fig. 16a and b. The 2-mm aperture with a 100- $\mu$ m thickness required ~22 kPa to achieve a 1-mm deflection, while the 0.5-mm aperture with a 10- $\mu$ m thickness required ~145 kPa to reach a 0.5-mm deflection.

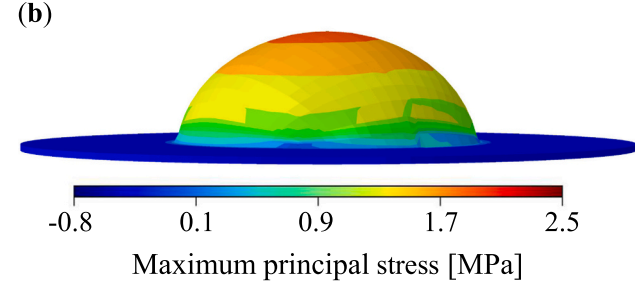
Each model was simulated under incremental pressure loading until the threshold stress, which defines the rupture limit for each membrane thickness, was reached. Meanwhile, both the maximum principal stress and membrane deflection ( $w_{max}$ ) were recorded. The maximum principal stress increased steadily with pressure until reaching the threshold value. The corresponding  $d_{\text{max}}$  and required inflation pressure are exhibited in Figs. 16c and 16d. As expected, a larger aperture radius produces greater  $d_{\text{max}}$  under lower applied pressure, and a thinner membrane achieves larger  $d_{\text{max}}$  at a fixed aperture radius. These trends provide useful guidelines for selecting balloon size  $(w_{\text{max}})$  and inflation pressure for our device. For example, to achieve a balloon size exceeding 1 mm, an aperture radius of 2 mm was sufficient across all three thicknesses. In contrast, smaller apertures required thinner membranes to reach comparable deflections. The aperture radius of 1.5 mm required either a thickness of 10 or 40  $\mu m$ , and the aperture radius of 1 mm required 10 µm.

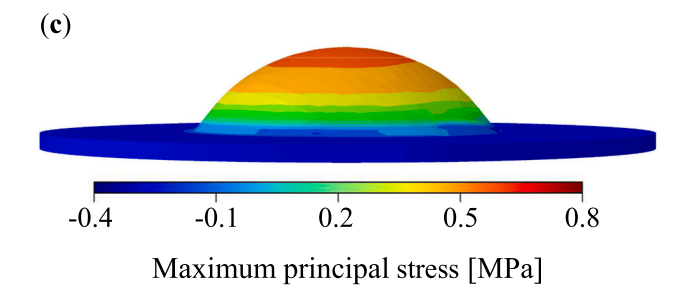
Collectively, our FE model may serve as a predictive tool for rational device design by estimating the maximum attainable microballoon sizes  $d_{\rm max}$ , one of the most important design factors, and the required inflation pressure, as a function of membrane thickness and aperture radius. Moreover, the simulation results identify stress concentration regions and safe operational limits, which are essential for minimizing rupture risk and enhancing device reliability.

# 3.6. Mixing performance evaluation

We assessed the mixing performance of the proposed ultrathin PDMS







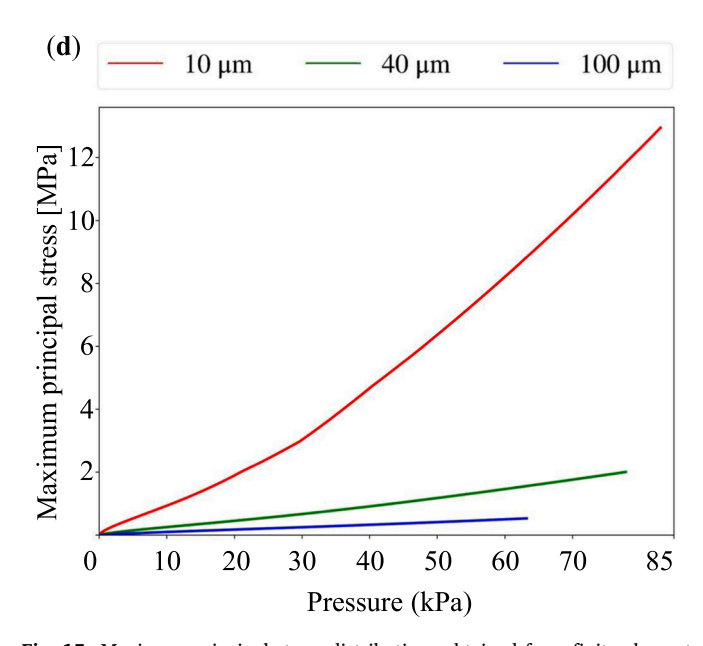
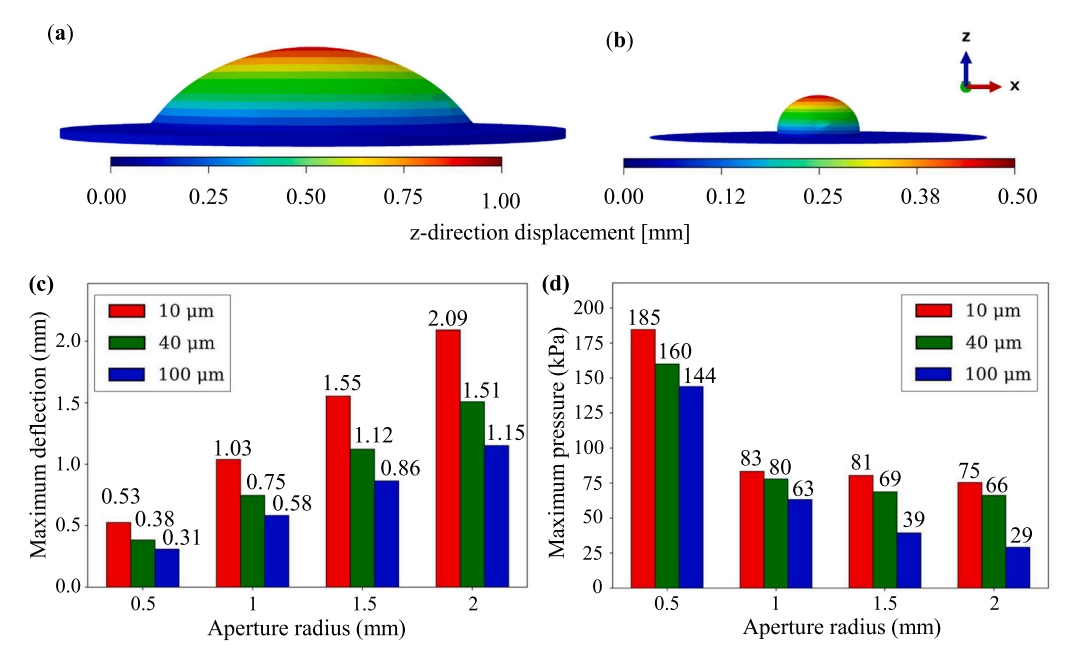


Fig. 15. Maximum principal stress distributions obtained from finite element analysis for membrane thicknesses of (a) 10  $\mu m$ , (b) 40  $\mu m$ , and (c) 100  $\mu m$  at the maximum applied pressure shown in Fig. 14. (d) The variation of maximum principal stress at the membrane apex as a function of applied pressure, up to the rupture point for each thickness.



**Fig. 16.** Finite element analysis results showing the influence of the aperture radius and membrane thickness on the pressure required to reach the maximum attainable deflection ( $d_{max}$ ) of inflated membranes. The  $d_{max}$  values were predicted at the threshold principal stress (obtained from Fig. 15d) as a function of aperture radius (0.5, 1, 1.5, and 2 mm) and membrane thickness (10, 40, and 100 μm). Two representative displacement contours show that (a) for an aperture radius of 2 mm and a membrane thickness of 100 μm, a pressure of ~22 kPa was required to reach a 1-mm deflection, and (b) for an aperture radius of 0.5 mm and a membrane thickness of 10 μm, ~145 kPa was required to achieve a 0.5-mm deflection. (c) Maximum attainable deflection  $d_{max}$  as a function of aperture radius for each membrane thickness and (d) corresponding inflation pressure required to achieve the  $d_{max}$  values.

microballoon oscillator (Fig. 17a) using the mixing index (MI) as a quantitative measure. Experiments were conducted under the optimized operating conditions (Section 3.4):  $h=40~\mu\text{m}$ ,  $V_{\text{exc}}=60~V_{\text{pp}}$ , and  $w_{\text{max}}=0.80~\text{mm}$ .

Under these conditions, a  $6-\mu L$  ink droplet was homogenized on a  $600-\mu L$  DI water within 32 s, reaching an MI of 0.82, which corresponds to 90% of the steady-state MI value (Fig. 16b). This rapid homogenization is particularly notable considering the 100-fold larger water volume relative to the ink volume. In contrast, the control experiment, where the balloon was inflated to the same size but left unactuated (Fig. 16c), reached only an MI of 0.54 over the same period.

These results highlight excellent mixing performance of our device, especially considering its relatively low active surface-to-volume ratio ( $R_{\rm sv}=5.24~{\rm m}^{-1}$ ) obtained using a single 2-mm-diameter microballoon to mix an ample 600-µL water volume. For comparison, prior work based on cavitation microstreaming achieved effective mixing by utilizing a much higher  $R_{\rm sv}$  value of 137 m<sup>-1</sup> utilizing 35 air pockets of 0.5-mm diameter to mix only 50- µL liquid [109].

#### 3.7. Cell lysis and DNA extraction

# 3.7.1. Experimental details

The cell lysis and DNA extraction protocol was adapted from our previous study [29], with modifications tailored to the present device configuration. Briefly, Mixture I (ethanol and magnetic beads) and Mixture II (a combination of cell suspension, lysis buffer, and Proteinase K) were sequentially loaded into a thoroughly cleaned cylindrical container (Fig. 2b). Mixture I and II were prepared off-chip in microcentrifuge tubes ( $\sim$ 3 s each) and promptly loaded into the device ( $\sim$ 7 s). The container was then sealed with PCR tape to prevent evaporation or leakage during agitation.

Upon excitation at the predetermined resonance frequency ( $\sim$ 6.1 kHz) using 60 V<sub>pp</sub>, the PDMS microballoon at the container bottom generated strong out-of-plane, counter-rotating circulatory flows, effectively mixing the reagents within the chamber. DNA-bound silicacoated magnetic beads were subsequently collected into a compact

cluster against the container wall using a neodymium magnet. Following bead collection, residual intracellular components (e.g., RNA, proteins, lipids) were removed via micropipette aspiration. Images for key steps in the workflow are exhibited in Fig. S10. Subsequent stages, including reagent loading, mixing, bead collection, waste removal, and DNA elution, followed a similar procedure as described in Section 2.9.

Minimizing assay time is essential for high-throughput applications. Through brief experimental optimization, the following durations were selected: 5 min for cell lysis, 1.5 min for washing, and 10 min for DNA elution. The total assay time from Mixture I loading to DNA elution was 18 min. This represents a more than threefold improvement in throughput compared to the commercial MagaZorb DNA Mini-Prep Kit, which requires 60 min per the manufacturer's protocol [110]. Moreover, our method outperformed previously reported microfluidic systems for chemical lysis and DNA extraction in terms of assay throughput, including our own earlier work (typically 20–25 min [29,111]). Additional reductions in assay time may be achievable by further optimizing the mixing durations at each step.

#### 3.7.2. DNA-extraction performance analysis

The performance of the microballoon oscillator for cell lysis and DNA extraction was evaluated using the K562 cell. K562, a human chronic myeloid leukemia cell line, is widely used in biomedical research for investigating fundamental biological processes and serves as a model system for cancer studies [112]. This cell line has been also employed in large-scale CRISPR/Cas9 gene-targeting screens [112] and in-vitro target screening for cancer drugs via flow cytometry [113].

The DNA concentration extracted using our device was 12.8  $\pm$  0.21 ng/µL (n=5, injected cells = 1.26  $\times$  10°), and that obtained with a commercial kit (MagaZorb DNA Mini-Prep Kit) was 13.6  $\pm$  0.17 ng/µL (n=5). The DNA purity (A260/A280) was 1.96  $\pm$  0.06 for our device and 1.98  $\pm$  0.21 for the commercial kit (Table 2), both within the acceptable range (1.7–2.0). On average, our device achieved 94.1 % of the DNA yield compared to the commercial kit, while maintaining high purity suitable for downstream applications. The DNA yield is superior to our previous DNA extraction device based on cavitation

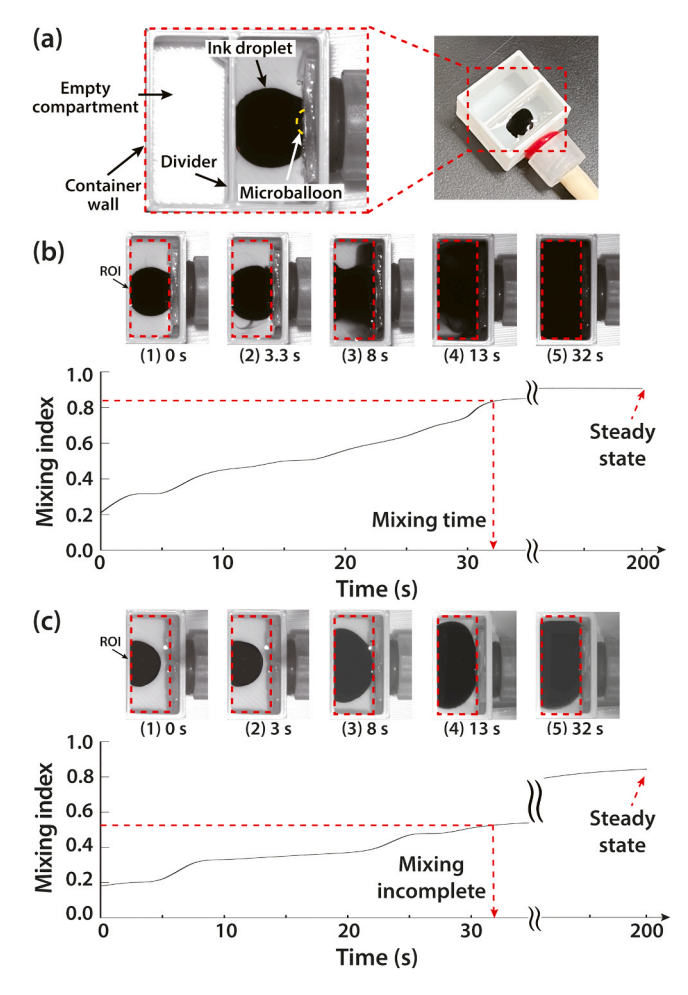


Fig. 17. Mixing performance of the ultrathin PDMS microballoon oscillator. (a) Mixing of a 6- $\mu$ l ink droplet in a 600- $\mu$ l DI water represented by the mixing index (MI) over time. With acoustic agitation, mixing was completed within 32 s (MI = 0.82), and (b) without agitation, mixing remained incomplete at the same time point (MI = 0.54). The red dotted boxes indicate regions of interests (ROI) used for MI calculation.

**Table 2**DNA extraction performance of the PDMS microballoon oscillator compared to a commercial kit.

Method	DNA concentration (ng/µl)	Purity (A <sub>260</sub> /A <sub>280</sub> )	Chip-to-kit concentration ratio
Microballoon oscillator	$12.8 \pm 0.21^{\text{a}}$	$1.96 \pm 0.06$	0.941
MagaZorb DNA Mini- prep kit	$13.6 \pm 0.17$	$1.98 \pm 0.21$	

 $<sup>^</sup>a$  adjusted by a factor of 0.5 for reduced elution volume (100  $\mu L$  vs. 200  $\mu L$  for the commercial kit).

microstreaming (84.9%) [29]. These results indicate that the performance of our device is comparable to that of the commercial kit in terms of DNA quantity and quality.

A control experiment was conducted under identical conditions but using an uninflated PDMS membrane. The DNA yield dropped significantly to  $8.85\pm0.11$  ng/µL (n=5), corresponding to only 69.1 % of the yield achieved with the inflated microballoon, confirming the critical contribution of acoustic streaming using an inflated membrane to the lysis and extraction process (see Section 3.4.4).

While the results are promising as a proof-of-concept, the DNA yield was slightly below that of the commercial kit. This discrepancy may be

attributed to suboptimal assay protocols or device design. The primary aim of this study was to demonstrate the feasibility of employing an ultrathin PDMS microballoon for acoustic-streaming-assisted cell lysis and DNA extraction, rather than to achieve fully optimized performance. One design-related factor is the relatively low active surface-to-volume ratio ( $R_{\rm sv}=31.4~{\rm m}^{-1}$ ), as only a single 2-mm-diameter microballoon was used to agitate a 100-µL solution. In our previous work, DNA extraction efficiency reached 84.9 % of commercial kits when  $R_{\rm sv}$  value was 17 m<sup>-1</sup> [29]. These findings suggest that performance could be further enhanced by using a larger balloon diameter (as long as it can fit within the container) or an array of multiple balloons (e.g., 3 × 3 or 4 × 4), thereby increasing  $R_{\rm sv}$  and enhancing mixing efficiency.

#### 3.7.3. PCR and gel electrophoresis results

The DNA extraction performance was further assessed through PCR amplification and gel electrophoresis. For comparison, genomic DNAs from K562 cells extracted using our device and a commercial kit were amplified for the von Willebrand factor (vWF) gene and analyzed via agarose gel electrophoresis. The results are exhibited in Fig. 18, along with a negative control (DI water, lane 4).

A distinct band at 116 base pairs (bp) in lane 3 confirms that DNA extracted using our device has sufficient quality for downstream applications. A positive-control experiment using DNA extracted with the commercial kit produced a comparable gel electrophoresis result (lane 2), validating the reliability and effectiveness of our microballoon-based DNA extraction method. The absence of a band in the negative control verifies the lack of contamination or false-positive amplification.

These results demonstrate that our prototype can deliver comparable performance to standard commercial kits, while eliminating the need for a bulky vortex mixer and achieving threefold improvement in assay throughput. Given the compact form factor and reduced processing

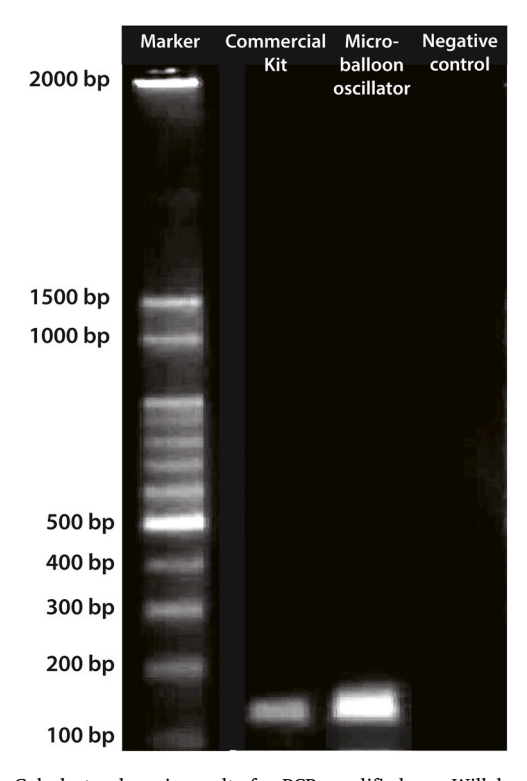


**Fig. 18.** Gel electrophoresis results for PCR-amplified von Willebrand factor (vWF) gene (116 bp) in genomic DNA extracted from K562 cells ( $\sim 1.26 \times 10^{\circ}$ ). DNA was extracted using the MagaZorb DNA Mini-Prep kit (positive control, lane 2) and our microballoon oscillator (lane 3). A negative control using DI water was included (lane 4). Distinct bands at 116-bp in lanes 2 and 3 confirm successful amplification. The absence of a band in lane 4 indicates the no contamination or false positives.

time, and ease of integration, we envision this platform as a promising candidate for portable, point-of-care nucleic acid analysis applications.

# 4. Conclusions

Microscale mixing is a fundamental aspect of microfluidic research due to its ubiquitous role in a wide range of applications. Among the explored strategies, acoustofluidic mixing offers controllable, effective mixing and straightforward integration into microfluidic platforms. In particular, cavitation microstreaming has garnered significant interest due to its exceptionally rapid mixing. However, its practical implementation is limited by the inherent instability of oscillating bubbles under acoustic excitation and their poor shelf-life during storage and transport.

In this work, we introduced a novel device architecture, an oscillating ultrathin PDMS microballoon, as a robust alternative. Our approach was inspired by the hypothesis that an oscillating ultrathin PDMS membrane could generate strong acoustic streaming while offering significantly improved operational lifetimes.

A solvent-free spin-coating process was developed to fabricate submicron PDMS membranes (860 nm) by optimizing only spin speed and duration. The membrane was then transferred permanently to a 3D-printed oscillator body to complete fabrication. The device was comprehensively characterized including the pressure-inflation characteristics and deflation behavior to evaluate performance and device lifetime, a critical factor for practical application. Operating parameters including membrane thickness, excitation voltage, and balloon size were optimized based on flow speed, streaming range, and device reliability. Notably, streaming remained effective for over 6 h even with a substantial balloon deflation. Furthermore, our finite element method based on the Yeoh hyperelastic model accurately predicted balloon size and identified stress concentrations, providing valuable design guidelines and safe operating limits.

Using this configuration, we demonstrated rapid mixing of a 6-µL ink droplet in a 100-fold larger volume of DI water within 32 s. Functional applicability was also evaluated via DNA extraction, yielding a concentration of 12.8 ng/µL and a purity of 1.96, comparable to those obtained using a commercial kit without extensive assay optimization. PCR and gel electrophoresis also validated the quality and downstream compatibility of the extracted DNA. Furthermore, the total assay time was only 18 min, a more than threefold improvement from a gold-standard commercial protocol. Due to its compact form factor and reduced assay time, our microballoon-based DNA extractor is well-suited for integration into portable, point-of-care molecular diagnostic platforms.

By overcoming the robustness limitation of cavitation microstreaming while achieving strong mixing, our ultrathin PDMS microballoon oscillator will offer a promising platform for integration into microfluidic systems requiring effective and robust mixing. Ongoing efforts focus on extending device lifetime using air-permeation barrier coatings (e.g., parylene C, Teflon) or surface modification (e.g.,  $O_2$  plasma treatment [95]), and enhancing mixing performance by integrating multiple oscillators in array formats. In addition, we will pursue theoretical investigations into microballoon-induced streaming to advance the fundamental understanding of the acoustic streaming mechanism and a structural modal analysis of the fully assembled device, aiming to maximize acoustic energy transfer and improve overall streaming performance.

# CRediT authorship contribution statement

Bhargav Krishna Pullagura: Validation, Methodology, Investigation. Heeyeon Kim: Validation, Methodology, Investigation, Data curation. Abdi Mirgissa Kaba: Validation, Methodology, Investigation. Dohyun Park: Validation, Methodology, Investigation. Taeksang Lee: Writing – original draft, Supervision, Resources, Project administration,

Investigation, Data curation, Conceptualization. **Dohyun Kim:** Writing – review & editing, Writing – original draft, Supervision, Resources, Project administration, Investigation, Funding acquisition, Data curation, Conceptualization. **Yeji Yang:** Writing – original draft, Visualization, Validation, Methodology, Investigation, Formal analysis, Data curation. **Changsub Shin:** Visualization, Validation, Methodology, Investigation, Formal analysis, Data curation. **Sofonias Nursefa Kedir:** Visualization, Validation, Methodology, Investigation, Data curation.

# Declaration of Generative AI and AI-assisted technologies in the writing process

During the preparation of this work the author(s) used ChatGPT in order to improve the readability and language of the manuscript. After using this tool/service, the author(s) reviewed and edited the content as needed and take(s) full responsibility for the content of the published article

#### **Declaration of Competing Interest**

The authors declare that they have no known competing financial interests or personal relationships that could have appeared to influence the work reported in this paper.

# Acknowledgements

This work was supported by Basic Science Research Programs (2021R1F1A1045386, 2022R1A2C1002729 and RS-2024–00339205) through the National Research Foundation of Korea (NRF).

# Appendix A. Supporting information

Supplementary data associated with this article can be found in the online version at doi:10.1016/j.snb.2025.139009.

# Data availability

Data will be made available on request.

#### References

- V. Hessel, H. Löwe, F. Schönfeld, Micromixers—a review on passive and active mixing principles, Chem. Eng. Sci. 60 (2005) 2479–2501, https://doi.org/ 10.1016/j.ces.2004.11.033.
- [2] Z. Li, Y. Bai, M. You, J. Hu, C. Yao, L. Cao, et al., Fully integrated microfluidic devices for qualitative, quantitative and digital nucleic acids testing at point of care, Biosens. Bioelectron. 177 (2021) 112952, https://doi.org/10.1016/j. bios.2020.112952.
- [3] K. Wu, X. He, J. Wang, T. Pan, R. He, F. Kong, et al., Recent progress of microfluidic chips in immunoassay, Front. Bioeng. Biotechnol. 10 (2022), https://doi.org/10.3389/fbioe.2022.1112327.
- [4] R. Pol, F. Céspedes, D. Gabriel, M. Baeza, Microfluidic lab-on-a-chip platforms for environmental monitoring, TrAC Trends Anal. Chem. 95 (2017) 62–68, https:// doi.org/10.1016/j.trac.2017.08.001.
- [5] L. Xia, J. Yang, R. Su, W. Zhou, Y. Zhang, Y. Zhong, et al., Recent progress in fast sample preparation techniques, Anal. Chem. 92 (2020) 34–48, https://doi.org/ 10.1021/acs.analchem.9b04735.
- [6] K.-A. Knapp, M.L. Nickels, H.C. Manning, The current role of microfluidics in radiofluorination chemistry, Mol. Imaging Biol. 22 (2020) 463–475, https://doi. org/10.1007/s11307-019-01414-6.
- [7] S. Gimondi, H. Ferreira, R.L. Reis, N.M. Neves, Microfluidic devices: a tool for nanoparticle synthesis and performance evaluation, ACS Nano 17 (2023) 14205–14228, https://doi.org/10.1021/acsnano.3c01117.
- [8] J. Jang, W.-S. Kim, T.S. Seo, B.J. Park, Over a decade of progress: crystallization in microfluidic systems, Chem. Eng. J. 495 (2024) 153657, https://doi.org/ 10.1016/j.cej.2024.153657.
- [9] I.M. Lazar, N.S. Gulakowski, A.C. Lazar, Protein and proteome measurements with microfluidic chips, Anal. Chem. 92 (2020) 169–182, https://doi.org/ 10.1021/acs.analchem.9b04711.
- [10] M. Adampourezare, G. Dehghan, M. Hasanzadeh, M.-A. Hosseinpoure Feizi, Application of lateral flow and microfluidic bio-assay and biosensing towards identification of DNA-methylation and cancer detection: recent progress and

- challenges in biomedicine, Biomed. Pharm. 141 (2021) 111845, https://doi.org/10.1016/j.biopha.2021.111845.
- [11] D.J. Beebe, G.A. Mensing, G.M. Walker, Physics and applications of microfluidics in biology, Annu. Rev. Biomed. Eng. 4 (2002) 261–286, https://doi.org/10.1146/ annurev.bioeng.4.112601.125916.
- [12] T.M. Squires, S.R. Quake, Microfluidics: fluid physics at the nanoliter scale, Rev. Mod. Phys. 77 (2005) 977–1026, https://doi.org/10.1103/RevModPhys.77.977.
- [13] Z. Li, B. Zhang, D. Dang, X. Yang, W. Yang, W. Liang, A review of microfluidic-based mixing methods, Sens. Actuators A Phys. 344 (2022) 113757, https://doi.org/10.1016/j.sna.2022.113757.
- [14] S.M. Saravanakumar, P.-V. Cicek, Microfluidic mixing: a physics-oriented review, Micromachines 14 (2023) 1827, https://doi.org/10.3390/mi14101827.
- [15] X. Wang, Z. Liu, B. Wang, Y. Cai, Q. Song, An overview on state-of-art of micromixer designs, characteristics and applications, Anal. Chim. Acta 1279 (2023) 341685, https://doi.org/10.1016/j.aca.2023.341685.
- [16] M. Bayareh, M.N. Ashani, A. Usefian, Active and passive micromixers: a comprehensive review, Chem. Eng. Process 147 (2020) 107771, https://doi.org/ 10.1016/j.cep.2019.107771.
- [17] S. Razavi Bazaz, A. Sayyah, A.H. Hazeri, R. Salomon, A. Abouei Mehrizi, M. Ebrahimi Warkiani, Micromixer research trend of active and passive designs, Chem. Eng. Sci. 293 (2024) 120028, https://doi.org/10.1016/j.ces.2024.120028.
- [18] K. Ward, Z.H. Fan, Mixing in microfluidic devices and enhancement methods, J. Micromech. Micro 25 (2015) 094001, https://doi.org/10.1088/0960-1317/ 25/9/094001.
- [19] C.-Y. Lee, W.-T. Wang, C.-C. Liu, L.-M. Fu, Passive mixers in microfluidic systems: a review, Chem. Eng. J. 288 (2016) 146–160, https://doi.org/10.1016/j. cej.2015.10.122.
- [20] S.P. Kee, A. Gavriilidis, Design and characterisation of the staggered herringbone mixer, Chem. Eng. J. 142 (2008) 109–121, https://doi.org/10.1016/j. cei.2008.02.001.
- [21] S. Hossain, M.A. Ansari, A. Husain, K.-Y. Kim, Analysis and optimization of a micromixer with a modified tesla structure, Chem. Eng. J. 158 (2010) 305–314, https://doi.org/10.1016/j.cej.2010.02.002.
- [22] D. Bahrami, M. Bayareh, Impacts of channel wall twisting on the mixing enhancement of a novel spiral micromixer, Chem. Pap. 76 (2022) 465–476, https://doi.org/10.1007/s11696-021-01876-5.
- [23] H.E.H. Meijer, M.K. Singh, T.G. Kang, J.M.J. den Toonder, P.D. Anderson, Passive and active mixing in microfluidic devices, Macromol. Symp. 279 (2009) 201–209, https://doi.org/10.1002/masy.200950530.
- [24] J.M. Ottino, S. Wiggins, Introduction: mixing in microfluidics, Philos. Trans. R. Soc. Lond. Ser. A (2004) 923–935, https://doi.org/10.1098/rsta.2003.1355.
- [25] Y. Li, S. Cai, H. Shen, Y. Chen, Z. Ge, W. Yang, Recent advances in acoustic microfluidics and its exemplary applications, Biomicrofluidics 16 (2022), https://doi.org/10.1063/5.0089051.
- [26] C.-C. Chang, R.-J. Yang, Electrokinetic mixing in microfluidic systems, Microfluid. Nanofluid 3 (2007) 501–525, https://doi.org/10.1007/s10404-007-0178-7
- [27] G. Cai, L. Xue, H. Zhang, J. Lin, A review on micromixers, Micromachines 8 (2017) 274, https://doi.org/10.3390/mi8090274.
   [28] T.J. Ober, D. Foresti, J.A. Lewis, Active mixing of complex fluids at the
- [28] T.J. Ober, D. Foresti, J.A. Lewis, Active mixing of complex fluids at the microscale, Proc. Natl. Acad. Sci. USA 112 (2015) 12293–12298, https://doi.org/ 10.1073/pnas.1509224112.
- [29] A.M. Kaba, H. Jeon, A. Park, K. Yi, S. Baek, A. Park, et al., Cavitation-microstreaming-based lysis and DNA extraction using a laser-machined polycarbonate microfluidic chip, Sens. Actuators B Chem. 346 (2021) 130511, https://doi.org/10.1016/i.snb.2021.130511.
- [30] J. Jalal, T.S.H. Leong, Microstreaming and its role in applications: a mini-review, Fluids 3 (2018) 93, https://doi.org/10.3390/fluids3040093.
- [31] W. Huang, Q. Yang, J. Liao, S. Ramadan, X. Fan, S. Hu, et al., Integrated Rayleigh wave streaming-enhanced sensitivity of shear horizontal surface acoustic wave biosensors, Biosens. Bioelectron. 247 (2024) 115944, https://doi.org/10.1016/j. bios.2023.115844
- [32] H. Jeon, K.A. Mirgissa, S. Baek, K. Rhee, D. Kim, Excitation-frequency determination based on electromechanical impedance spectroscopy for a lasermicrofabricated cavitation microstreaming micromixer, Sens. Actuators A Phys. 326 (2021) 112730, https://doi.org/10.1016/j.sna.2021.112730.
- [33] H. Ahmed, S. Ramesan, L. Lee, A.R. Rezk, L.Y. Yeo, On-chip generation of vortical flows for microfluidic centrifugation, Small 16 (2020) 1903605, https://doi.org/ 10.1002/smll.201903605.
- [34] S. Li, W. Cui, T. Baasch, B. Wang, Z. Gong, Eckart streaming with nonlinear highorder harmonics: an example at gigahertz, Phys. Rev. Fluids 9 (2024) 084201, https://doi.org/10.1103/PhysRevFluids.9.084201.
- [35] Z. Chen, P. Liu, X. Zhao, L. Huang, Y. Xiao, Y. Zhang, et al., Sharp-edge acoustic microfluidics: principles, structures, and applications, Appl. Mater. Today 25 (2021) 101239, https://doi.org/10.1016/j.apmt.2021.101239.
- [36] A.A. Doinikov, M.S. Gerlt, A. Pavlic, J. Dual, Acoustic streaming produced by sharp-edge structures in microfluidic devices, Microfluid. Nanofluid 24 (2020) 32, https://doi.org/10.1007/s10404-020-02335-5.
- [37] N. Nam-Trung, R.M. White, Acoustic streaming in micromachined flexural plate wave devices: numerical simulation and experimental verification, IEEE Trans. Ultrason. Ferroelectr. Freq. Control 47 (2000) 1463–1471, https://doi.org/ 10.1109/58.883536.
- [38] J.-C. Hsu, C.-Y. Chang, Enhanced acoustofluidic mixing in a semicircular microchannel using plate mode coupling in a surface acoustic wave device, Sens. Actuators A Phys. 336 (2022) 113401, https://doi.org/10.1016/j. sna.2022.113401.

- [39] H. Zhang, Z. Tang, Z. Wang, S. Pan, Z. Han, C. Sun, et al., Acoustic streaming and microparticle enrichment within a microliter droplet using a Lamb-wave resonator array, Phys. Rev. Appl. 9 (2018) 064011, https://doi.org/10.1103/ PhysRevApplied.9.064011.
- [40] J. Nam, W.S. Jang, J. Kim, H. Lee, C.S. Lim, Lamb wave-based molecular diagnosis using DNA hydrogel formation by rolling circle amplification (RCA) process, Biosens. Bioelectron. 142 (2019) 111496, https://doi.org/10.1016/j. bios.2019.111496.
- [41] X. Liu, X. Chen, Z. Yang, H. Xia, C. Zhang, X. Wei, Surface acoustic wave based microfluidic devices for biological applications, Sens. Diagn. 2 (2023) 507–528, https://doi.org/10.1039/D2SD00203E.
- [42] D. Mandal, S. Banerjee, Surface acoustic wave (SAW) sensors: physics, materials, and applications, Sensors 22 (2022) 820, https://doi.org/10.3390/s22030820.
- [43] M. Wiklund, R. Green, M. Ohlin, Acoustofluidics 14: applications of acoustic streaming in microfluidic devices, Lab Chip 12 (2012) 2438–2451, https://doi. org/10.1039/C2LC40203C.
- [44] J. Wu, Acoustic streaming and its applications, Fluids 3 (2018) 108, https://doi. org/10.3390/fluids3040108.
- [45] P. Zhang, H. Bachman, A. Ozcelik, T.J. Huang, Acoustic microfluidics, Annu. Rev. Anal. Chem. 13 (2020) 17–43, https://doi.org/10.1146/annurev-anchem-090919-102205.
- [46] A. Hashmi, G. Yu, M. Reilly-Collette, G. Heiman, J. Xu, Oscillating bubbles: a versatile tool for lab on a chip applications, Lab Chip 12 (2012) 4216–4227, https://doi.org/10.1039/C2LC40424A.
- [47] X. Liu, J. Wu, Acoustic microstreaming around an isolated encapsulated microbubble, J. Acoust. Soc. Am. 125 (2009) 1319–1330, https://doi.org/ 10.1121/1.3075552
- [48] A.A. Doinikov, A. Bouakaz, Acoustic microstreaming around a gas bubble, J. Acoust. Soc. Am. 127 (2010) 703–709, https://doi.org/10.1121/1.3279793
- [49] A.A. Doinikov, A. Bouakaz, Acoustic microstreaming around an encapsulated particle, J. Acoust. Soc. Am. 127 (2010) 1218–1227, https://doi.org/10.1121/ 1.2300007
- [50] L. Sun, T. Lehnert, S. Li, M.A.M. Gijs, Bubble-enhanced ultrasonic microfluidic chip for rapid DNA fragmentation, Lab Chip 22 (2022) 560–572, https://doi.org/ 10.1039/DJLC00933H
- [51] H. Chen, Y. Gao, K. Petkovic, S. Yan, M. Best, Y. Du, et al., Reproducible bubble-induced acoustic microstreaming for bead disaggregation and immunoassay in microfluidics, Microfluid. Nanofluid 21 (2017) 30, https://doi.org/10.1007/s10404-017-1870-2
- [52] R.H. Liu, J. Yang, M.Z. Pindera, M. Athavale, P. Grodzinski, Bubble-induced acoustic micromixing, Lab Chip 2 (2002) 151–157, https://doi.org/10.1039/ B201952C.
- [53] D. Ahmed, X. Mao, J. Shi, B.K. Juluri, T.J. Huang, A millisecond micromixer via single-bubble-based acoustic streaming, Lab Chip 9 (2009) 2738–2741, https:// doi.org/10.1039/B903687C.
- [54] L. Liu, C. Yao, S. Zhao, Z. Liu, G. Chen, Enhanced antisolvent processes in an ultrasonic capillary microreactor: cavitation, mixing and application in miniemulsion preparation, Chem. Eng. J. 466 (2023) 143426, https://doi.org/ 10.1016/j.cej.2023.143426.
- [55] P. Tho, R. Manasseh, A. Ooi, Cavitation microstreaming patterns in single and multiple bubble systems, J. Fluid Mech. 576 (2007) 191–233, https://doi.org/ 10.1017/S0022112006004393.
- [56] S. Seyedmirzaei Sarraf, F. Rokhsar Talabazar, I. Namli, M. Maleki, A. Sheibani Aghdam, G. Gharib, et al., Fundamentals, biomedical applications and future potential of micro-scale cavitation-a review, Lab Chip 22 (2022) 2237–2258, https://doi.org/10.1039/D2LC00169A.
- [57] A. Ozcelik, D. Ahmed, Y. Xie, N. Nama, Z. Qu, A.A. Nawaz, et al., An acoustofluidic micromixer via bubble inception and cavitation from microchannel sidewalls, Anal. Chem. 86 (2014) 5083–5088, https://doi.org/ 10.1021/ac5007798.
- [58] F.J. Jackson, W.L. Nyborg, Small scale acoustic streaming near a locally excited membrane, J. Acoust. Soc. Am. 30 (1958) 614–619, https://doi.org/10.1121/ 1.1909712
- [59] H.V. Phan, T. Alan, A. Neild, Droplet manipulation using acoustic streaming induced by a vibrating membrane, Anal. Chem. 88 (2016) 5696–5703, https:// doi.org/10.1021/acs.analchem.5b04481.
- [60] H.V. Phan, M.B. Coşkun, M. Şeşen, G. Pandraud, A. Neild, T. Alan, Vibrating membrane with discontinuities for rapid and efficient microfluidic mixing, Lab Chip 15 (2015) 4206–4216, https://doi.org/10.1039/C5LC00836K.
- [61] L.-S. Jang, S.-H. Chao, M.R. Holl, D.R. Meldrum, Microfluidic circulatory flows induced by resonant vibration of diaphragms, Sens. Actuators A Phys. 122 (2005) 141–148, https://doi.org/10.1016/j.sna.2005.03.070.
- [62] R.D. James, J.W. Jacobs, A. Glezer, A round turbulent jet produced by an oscillating diaphragm, Phys. Fluids 8 (1996) 2484–2495, https://doi.org/ 10.1063/1.869040.
- [63] Thermoplastics Physical Properties. (https://www.engineeringtoolbox.com/physical-properties-thermoplastics-d\_808.html), (accessed September 17, 2024).
- [64] H. Pierson, Handbook of chemical vapor deposition: principles, technology, and applications, Noyes Publications, New Jersey, 1999.
- [65] E.J. Boyd, D. Uttamchandani, Measurement of the anisotropy of young's modulus in single-crystal silicon, J. Micro Syst. 21 (2012) 243–249, https://doi.org/ 10.1109/JMEMS.2011.2174415.
- [66] S. Ahmad, S. Bashir, M.S. Rafique, D. Yousaf, Modifications in surface, structural and mechanical properties of brass using laser induced ni plasma as an ion source, AIP Adv. 6 (2016), https://doi.org/10.1063/1.4944663.

- [67] M. Liu, J. Sun, Y. Sun, C. Bock, Q. Chen, Thickness-dependent mechanical properties of polydimethylsiloxane membranes, J. Micromech. Micro 19 (2009) 035028, https://doi.org/10.1088/0960-1317/19/3/035028.
- [68] I.D. Johnston, D.K. McCluskey, C.K.L. Tan, M.C. Tracey, Mechanical characterization of bulk sylgard 184 for microfluidics and microengineering, J. Micromech. Micro 24 (2014) 035017, https://doi.org/10.1088/0960-1317/ 24/3/035017
- [69] J. Gao, D. Guo, S. Santhanam, G.K. Fedder, Material characterization and transfer of large-area ultra-thin polydimethylsiloxane membranes, J. Micro Syst. 24 (2015) 2170–2177, https://doi.org/10.1109/JMEMS.2015.2480388.
- [70] Y.N. Cheung, N.T. Nguyen, T.N. Wong, Droplet manipulation in a microfluidic chamber with acoustic radiation pressure and acoustic streaming, Soft Matter 10 (2014) 8122–8132, https://doi.org/10.1039/C4SM01453G.
- [71] N.F. Läubli, M.S. Gerlt, A. Wüthrich, R.T.M. Lewis, N. Shamsudhin, U. Kutay, et al., Embedded microbubbles for acoustic manipulation of single cells and microfluidic applications, Anal. Chem. 93 (2021) 9760–9770, https://doi.org/10.1021/10.1021/acs.analchem.1c01209.
- [72] S.-K. Chae, J.-H. Ryoo, S.-H. Lee, Thin and large free-standing PDMS membrane by using polystyrene petri dish, Biochip J. 6 (2012) 184–190, https://doi.org/ 10.1007/s13206-012-6211-7
- [73] M.L. Rathod, J. Ahn, B. Saha, P. Purwar, Y. Lee, N.L. Jeon, et al., PDMS sylgard 527-based freely suspended ultrathin membranes exhibiting mechanistic characteristics of vascular basement membranes, ACS Appl. Mater. Interfaces 10 (2018) 40388–40400, https://doi.org/10.1021/acsami.8b12309.
- [74] E. Kang, J. Ryoo, G.S. Jeong, Y.Y. Choi, S.M. Jeong, J. Ju, et al., Large-scale, ultrapliable, and free-standing nanomembranes, Adv. Mater. 25 (2013) 2167–2173, https://doi.org/10.1002/adma.201204619.
- [75] G.L. Jadav, V.K. Aswal, H. Bhatt, J.C. Chaudhari, P.S. Singh, Influence of film thickness on the structure and properties of PDMS membrane, J. Membr. Sci. 415-416 (2012) 624–634, https://doi.org/10.1016/j.memsci.2012.05.043.
- [76] J.H. Koschwanez, R.H. Carlson, D.R. Meldrum, Thin PDMS films using long spin times or tert-butyl alcohol as a solvent, PLoS One 4 (2009) e4572, https://doi. org/10.1371/journal.pone.0004572.
- [77] R. Pezzilli, G. Prestopino, N.A. Montoya, C. Leonardi, U. Khan, P.G. Medaglia, et al., Thin PDMS-on-sacrificial-PCB devices, ACS Appl. Electron. Mater. 4 (2022) 4490–4498, https://doi.org/10.1021/acsaelm.2c00734.
- [78] W.F. Quirós-Solano, N. Gaio, O.M.J.A. Stassen, Y.B. Arik, C. Silvestri, N.C.A. Van Engeland, et al., Microfabricated tuneable and transferable porous PDMS membranes for Organs-on-Chips, Sci. Rep. 8 (2018) 13524, https://doi.org/ 10.1038/s41598-018-31912-6.
- [79] M.M. Keshtiban, M.M. Zand, A. Ebadi, Z. Azizi, PDMS-based porous membrane for medical applications: design, development, and fabrication, Biomed. Mater. 18 (2023) 045012, https://doi.org/10.1088/1748-605X/acbddb.
- [80] A.L. Thangawng, R.S. Ruoff, M.A. Swartz, M.R. Glucksberg, An ultra-thin PDMS membrane as a bio/micro-nano interface: fabrication and characterization, Biomed. Micro 9 (2007) 587–595, https://doi.org/10.1007/s10544-007-9070-6.
- [81] GrabCAD (https://grabcad.com/library?page=1&per\_page=100&time=all\_time &sort=recent&query=luer), (accessed 12 September 2024).
- [82] S. Razavi Bazaz, N. Kashaninejad, S. Azadi, K. Patel, M. Asadnia, D. Jin, et al., Rapid softlithography using 3D-printed molds, Adv. Mater. Technol. 4 (2019) 1900425. https://doi.org/10.1002/admt.201900425.
- [83] B. Venzac, S. Deng, Z. Mahmoud, A. Lenferink, A. Costa, F. Bray, et al., PDMS curing inhibition on 3D-printed molds: why? Also, how to avoid it? Anal. Chem. 93 (2021) 7180–7187. https://doi.org/10.1021/acs.analchem.0c04944.
- [84] D. Meyerhofer, Characteristics of resist films produced by spinning, J. Appl. Phys. 49 (1978) 3993–3997, https://doi.org/10.1063/1.325357.
- [85] S. Granick, Z. Lin, S.C. Bae, Molecules squeezed and stroked, Nature 425 (2003) 467–468, https://doi.org/10.1038/425467a.
- [86] J. E. Ribeiro, H. Lopes, P. Martins, M. Braz-César, Mechanical analysis of PDMS material using biaxial test, AIMS Mater. Sci. 6 (2019) 97–110, https://doi.org/ 10.3934/matersci.2019.1.97.
- [87] Z. Li, Y. Wang, J. Xiao, Mechanics of curvilinear electronics and optoelectronics, Curr. Opin. Solid State Mater. Sci. 19 (2015) 171–189, https://doi.org/10.1016/j. cossms.2015.01.003.
- [88] O.H. Yeoh, Some forms of the strain energy function for rubber, Rubber Chem. Technol. 66 (1993) 754–771, https://doi.org/10.5254/1.353834.
- [89] A. Müller, M.C. Wapler, U. Wallrabe, A quick and accurate method to determine the poisson's ratio and the coefficient of thermal expansion of PDMS, Soft Matter 15 (2019) 779–784, https://doi.org/10.1039/C8SM02105H.
- [90] F.L. Givens, W.J. Daughton, On the uniformity of thin films: a new technique applied to polyimides, J. Electrochem. Soc. 126 (1979) 269, https://doi.org/ 10.1149/1.2129019
- [91] A.G. Emslie, F.T. Bonner, L.G. Peck, Flow of a viscous liquid on a rotating disk, J. Appl. Phys. 29 (1958) 858–862, https://doi.org/10.1063/1.1723300.
- [92] J. Tong, C.A. Simmons, Y. Sun, Precision patterning of PDMS membranes and applications, J. Micromech. Micro 18 (2008) 037004, https://doi.org/10.1088/ 0960-1317/18/3/037004.
- [93] J.Y. Park, D.H. Lee, E.J. Lee, S.-H. Lee, Study of cellular behaviors on concave and convex microstructures fabricated from elastic PDMS membranes, Lab Chip 9 (2009) 2043–2049, https://doi.org/10.1039/B820955C.
- [94] G.C. Randall, P.S. Doyle, Permeation-driven flow in poly(dimethylsiloxane) microfluidic devices, Proc. Natl. Acad. Sci. USA 102 (2005) 10813–10818, https://doi.org/10.1073/pnas.0503287102.
- [95] D.A. Markov, E.M. Lillie, S.P. Garbett, L.J. McCawley, Variation in diffusion of gases through PDMS due to plasma surface treatment and storage conditions, Biomed. Micro 16 (2014) 91–96, https://doi.org/10.1007/s10544-013-9808-2.

- [96] T.C. Merkel, V.I. Bondar, K. Nagai, B.D. Freeman, I. Pinnau, Gas sorption, diffusion, and permeation in poly(dimethylsiloxane), J. Polym. Sci. Part B Polym. Phys. 38 (2000) 415–434, https://doi.org/10.1002/(SICI)1099-0488(20000201) 38:3<415::AID-POLB8>3.0.CO;2-Z.
- [97] H. Ren, H.-S. Lee, J. Chae, Miniaturizing microbial fuel cells for potential portable power sources: promises and challenges, Microfluid. Nanofluid 13 (2012) 353–381, https://doi.org/10.1007/s10404-012-0986-7.
- [98] A. Javaid, Membranes for solubility-based gas separation applications, Chem. Eng. J. 112 (2005) 219–226, https://doi.org/10.1016/j.cej.2005.07.010.
- [99] Y. Lee, Y.-J. Park, J. Lee, T.-H. Bae, Recent advances and emerging applications of membrane contactors, Chem. Eng. J. 461 (2023) 141948, https://doi.org/ 10.1016/j.cej.2023.141948
- [100] M. Bora, M. Shusteff, Efficient coupling of acoustic modes in microfluidic channel devices, Lab Chip 15 (2015) 3192–3202, https://doi.org/10.1039/C5LC00343A.
- [101] H.N. Açıkgöz, A. Karaman, M.A. Şahin, Ö.R. Çaylan, G.C. Büke, E. Yıldırım, et al., Assessment of silicon, glass, FR4, PDMS and PMMA as a chip material for acoustic particle/cell manipulation in microfluidics, Ultrasonics 129 (2023) 106911, https://doi.org/10.1016/j.ultras.2022.106911.
- [102] W.H. Ko, B. Min-Hang, H. Yeun-Ding, A high-sensitivity integrated-circuit capacitive pressure transducer, IEEE Trans. Electron Devices 29 (1982) 48–56, https://doi.org/10.1109/T-ED.1982.20657.
- [103] M. Liu, J. Sun, Q. Chen, Influences of heating temperature on mechanical properties of polydimethylsiloxane, Sens. Actuators A Phys. 151 (2009) 42–45, https://doi.org/10.1016/j.sna.2009.02.016.
- [104] M.D. McKay, R.J. Beckman, W.J. Conover, A comparison of three methods for selecting values of input variables in the analysis of output from a computer code, Technometrics 42 (2000) 55–61, https://doi.org/10.2307/1268522.
- [105] J. Kennedy, R. Eberhart, Particle swarm optimization, Proc. ICNN'95Int. Conf. Neural Netw. 4 (1995) 1942–1948, https://doi.org/10.1109/ICNN.1995.488968.
- [106] Y. Shi, R. Eberhart, A modified particle swarm optimizer. 1998 IEEE international conference on evolutionary computation proceedings. IEEE world congress on computational intelligence, IEEE, Anchorage, AK, United States, 1998, pp. 69–73.
   [107] L.G. Treloar, The physics of rubber elasticity. Oxford University Press, New York,
- [107] L.G. Treloar, The physics of rubber elasticity, Oxford University Press, New York 1975.
- [108] A.P.S. Selvadurai, Mechanics of pressurized planar hyperelastic membranes, Philos. Trans. R. Soc. A 380 (2022) 20210319, https://doi.org/10.1098/ rsta.2021.0319.
- [109] R.H. Liu, R. Lenigk, R.L. Druyor-Sanchez, J. Yang, P. Grodzinski, Hybridization enhancement using cavitation microstreaming, Anal. Chem. 75 (2003) 1911–1917, https://doi.org/10.1021/ac026267t.
- [110] Promega, Genomic DNA extraction kits. http://www.promega.kr/en/products/nucleic-acid-extraction/genomic-dna/genomic-dna-extraction-kits/, 2021 (accessed 02 July 2021). https://www.promega.kr/en/products/nucleic-acid-extraction/genomic-dna/genomic-dna-extraction-kits/, (accessed 02 July).
- [111] X. Chen, D.F. Cui, C.C. Liu, On-line cell lysis and DNA extraction on a microfluidic biochip fabricated by microelectromechanical system technology, Electrophoresis 29 (2008) 1844–1851. https://doi.org/10.1002/elps.200700551.
- [112] B. Zhou, S.S. Ho, S.U. Greer, X. Zhu, J.M. Bell, J.G. Arthur, et al., Comprehensive, integrated, and phased whole-genome analysis of the primary ENCODE cell line K562, Genome Res 29 (2019) 472–484, https://doi.org/10.1101/gr.234948.118.
- [113] T. Inoue, A. Swain, Y. Nakanishi, D. Sugiyama, Multicolor analysis of cell surface marker of human leukemia cell lines using flow cytometry, Anticancer Res 34 (2014) 4539–4550.

Yeji Yang is a master's degree student in the Division of Mechanical Systems Engineering at Myongji University, South Korea. She received her B.S degree in Mechanical Engineering from the same University in 2024. She is in her third semester and is expecting to graduate in 2026. Her research interests include microfluidics, MEMS, and microfabrication, with a particular focus on acoustofluidic mixing through cavitation microstreaming.

Changsub Shin is currently an M.S. student in the Division of Mechanical Systems Engineering at Myongji University. He earned his B.S. degree in Mechanical Engineering from Myongji University in 2025. His research interests include developing in-house code based on the finite element method and conducting structural analysis simulations.

Sofonias Nursefa Kedir is a third-year combined M.S. and Ph.D. student in the Division of Mechanical Systems Engineering at Myongji University, South Korea. He received his B.S. degree in Mechanical Engineering from Addis Ababa University, Ethiopia, in 2020. He is currently a research assistant in the BioNanofluidics and Microfluidics Laboratory (BNML). His research focuses on microfluidic lab-on-a-chip devices for biomolecular analysis and adhesive-assisted laser microfabrication of microfluidic chips, designed to use acoustic streaming for DNA extraction.

Bhargav Krishna Pullagura is a postdoctoral researcher in the BioNanofluidics and Microfluidics Laboratory (BNML) at Myongji University, South Korea. He earned a B.Tech. in Chemical Engineering from the National Institute of Technology Warangal, India, in 2011, followed by M.Tech. and Ph.D. degrees in Chemical Engineering from the Indian Institute of Technology Bombay, India, in 2020. He then worked as a research associate at the same institution and later in in the Nano Bio Photonics Laboratory at Chung-Ang University, South Korea. His research interests include electrohydrodynamics in microfluidics, microfluidic synthesis of microfiber and microgel particles for antibacterial and drug-delivery applications, digital polymerase chain reaction (PCR), and microfluidic devices for biosensing.

**Heeyeon Kim** is an automation engineer at Sebang Global Battery. She received her B.S. degree in Mechanical Engineering from Myongil University in 2023. Her research concentrated on microfluidics, specifically on the fabrication of ultrathin PDMS film for use in 3D-printed acoustic streaming mixers.

Abdi Mirgissa Kaba is a postdoctoral researcher at the Paul Pascal Research Center, affiliated with the French National Centre for Scientific Research (CNRS), France. He received his B.S. and M.S. degrees in Mechanical Engineering from Addis Ababa University, Ethiopia, in 2015 and 2017, respectively. He completed his Ph.D. in Mechanical Engineering at Myongji University, South Korea, in 2022 and subsequently worked as a postdoctoral researcher in the BioNanofluidics and Microfluidics Laboratory (BNML) at the same university. His research focuses on microfluidic lab-on-a-chip devices for biomolecular analysis, droplet-based microfluidics for directed enzyme evolution, 3D printing of acoustic micromixers, and rapid prototyping of thermoplastic microfluidic devices.

**Dohyun Park** is a design engineer at LS Electric. He received a B.S. degree in Mechanical Engineering at Myongji University in 2025. His research focused on microfluidic chips, particularly the development of a 3D- printed micro-mixer with sharp-edge acoustic streaming.

Taeksang Lee is an assistant professor in the Division of Mechanical Systems Engineering at Myongji University. Before joining Myongji University, he worked as a staff engineer at Samsung Electronics from 2020 to 2021. He earned his B.S. and M.S. degrees in Mechanical Engineering from Sungkyunkwan University in 2014 and 2016, respectively, and his Ph.D. in Mechanical Engineering from Purdue University. His research interests focus on computational biomechanics based on continuum mechanics, machine learning, and multi-physics modeling and simulation.

Dohyun Kim is a professor and the chair of the Division of Mechanical Systems Engineering at Myongji University, South Korea. He earned his Ph.D. in Electrical Engineering from the University of California, Los Angeles, USA, in 2008. Before joining Myongji University in 2012, he was a postdoctoral scholar at the California Institute for Quantitative Biosciences, at University of California, Berkeley, and the Center for Embedded Networked Sensing at University of California, Los Angeles. He received 17 government or company-funded research grants, filed 19 patents, published 57 conference papers, advised 24 undergraduate and 17 graduate students, and delivered 28 invited talks. His research interests include polymer microfabrication, microfluidics, and molecular and protein-based point-of-care diagnostics.